

Channeling of protons through carbon nanotubes

Duško Borika, Srdjan Petrović and Nebojša Nešković
 Laboratory of Physics (010), Vinča Institute of Nuclear Sciences,
 P. O. Box 522, 11001 Belgrade, Serbia

Contents

Abstract	3
1 Introduction	4
2 Ion channeling	7
3 Crystal rainbows	10
3.1 Discovery of crystal rainbows	12
3.2 Theory of crystal rainbows	12
4 Zero-degree focusing of protons channeled through bundles of nanotubes	15
5 Angular distributions and rainbows in proton channeling through nanotubes	20
5.1 Rainbows with a straight very short bundle of nanotubes . . .	20
5.2 Rainbows with a bent short bundle of nanotubes	26
5.3 Rainbows with long nanotubes	30
6 Dynamic polarization effect in proton channeling through short nanotubes	35
6.1 Rainbows with short nanotubes in vacuum	36
6.2 Rainbows with short nanotube embedded in dielectric media .	39
6.3 Donut effect with protons and a short nanotube in vacuum . .	42

7	Dynamic polarization effect in proton channeling through short nanotubes	46
	References	53

Abstract

This book contains a thorough theoretical consideration of the process of proton channeling through carbon nanotubes. We begin with a very brief summary of the theoretical and experimental results of studying ion channeling through nanotubes. Then, the process of ion channeling is described briefly. After that, the crystal rainbow effect is introduced. We describe how it was discovered, and present the theory of crystal rainbows, as the proper theory of ion channeling in crystals and nanotubes. We continue with a description of the effect of zero-degree focusing of protons channeled through nanotubes. It is shown that the evolution of the angular distribution of channeled protons with the nanotube length can be divided in the cycles defined by the rainbow effect. Further, we analyze the angular distributions and rainbows in proton channeling through nanotubes. This is done using the theory of crystal rainbows. The angular distributions are generated by the computer simulation method, and the corresponding rainbow patterns are obtained in a precise analysis of the mapping of the impact parameter plane to the transmission angle plane. We demonstrate that the rainbows enable the full explanation of the angular distributions. The analysis demonstrates that the angular distributions contain the information on the transverse lattice structure of the bundle. In this study we investigate the rainbows in transmission of protons of the kinetic energy of 1 GeV through a straight very short bundle of (10, 10) single-wall carbon nanotube, a bent short bundle of (10, 10) nanotubes, and the straight long (11, 9) nanotubes.

We also investigate how the effect of dynamic polarization of the carbon atoms valence electrons influences the angular and spatial distributions of protons transmitted through short nanotubes in vacuum and embedded in dielectric media. It is demonstrated that this effect can induce the additional rainbow maxima in the angular distributions. We have established that the changing of the spatial distribution with the proton kinetic energy, based on the changing of the dynamic polarization effect, may be used to probe the atoms or molecules intercalated in the nanotubes. In these study we investigate the rainbows in transmission of 0.223-2.49 MeV protons through the short (11, 9) nanotubes in vacuum and embedded in SiO₂, Al₂O₃ and Ni. Besides, we report on the donut effect in transmission of 0.223 MeV protons through a short (11, 9) nanotube, which occurs when the initial ion velocity vector is not parallel to the nanotube axis. In addition, we explore the channeling star effect in 1 GeV proton channeling through bundles of

nanotubes, which appears when the proton beam divergence angle is larger than the critical angle for channeling.

1 Introduction

Carbon nanotubes were discovered by Iijima in 1991 (Iijima, 1991). One can describe them as the sheets of carbon atoms rolled up into the cylinders with the atoms lying at the hexagonal crystal lattice sites. The diameters of nanotubes are of the order of a nanometer and their lengths can be more than a hundred micrometers. Nanotubes can be the single-wall and multi-wall ones, depending on the number of cylinders they include. They have remarkable geometrical and physical properties (Saito et al., 2001). As a result, nanotubes have begun to play an important role in the field of nanotechnologies. For example, they are expected to become the basic elements for creating nanoelectronic devices (Yao et al., 1999).

The structure of a carbon nanotube is described by vector $\vec{C}_h = m\vec{a}_1 + n\vec{a}_2 \equiv (m, n)$, where \vec{a}_1 and \vec{a}_2 are the unit vectors of the hexagonal crystal lattice, and the integers satisfying inequalities $0 \leq |n| \leq m$ (Saito et al., 2001). This vector is called the chiral vector of the nanotube. Its magnitude is $C_h = (m^2 + mn + n^2)^{\frac{1}{2}}a_h$, where a_h is the magnitude of \vec{a}_1 and \vec{a}_2 . The angle of \vec{C}_h relative to \vec{a}_1 , which is called the chiral angle of the nanotube, is given by expression $\cos \Theta_h = (m + n/2)/(m^2 + mn + n^2)^{\frac{1}{2}}$ and inequalities $0 \leq |\Theta_h| \leq \pi/6$. This is shown in Fig. 1. The sheet of carbon atoms is rolled up into the cylinder in such a way to transform the segment corresponding to \vec{C}_h into a circle. Hence, the nanotube diameter equals \vec{C}_h/π . The nanotube is achiral or chiral. If it is achiral, the nanotube consists of the atomic strings parallel to its axis. In particular, if $n = 0$, when $\Theta_h = 0$, or $m = n$, when $\Theta_h = \pi/6$, the nanotube is achiral. In accordance with the shape of its transverse cross-section, in the former case the nanotube is called the zigzag one, and in the latter case the armchair one. If it is chiral, the nanotube consists of the atomic strings that spiral around its axis. This is illustrated in Fig. 2, which is taken from Ref. Saito et al. (2001).

Soon after the discovery of carbon nanotubes, Klimov and Letokhov (Klimov & Letokhov, 1996) predicted that they could be used to channel positively charged particles. After that, a number of theoretical groups have studied ion channeling through nanotubes (Gevorgian et al., 1998; Zhevago & Glebov, 1998; Biryukov & Bellucci, 2002; Greenenko & Shulga, 2003; Zhevago & Glebov,

2003; Artru et al., 2005; Bellucci et al., 2005; Krasheninnikov & Nordlund, 2005; Moura & Amaral, 2005; Borcka et al., 2005; Nešković et al., 2005; Petrović et al., 2005a,b; Borcka et al., 2006a,b, 2007; Matyukhin & Frolenkov, 2007; Mišković, 2007; Moura & Amaral, 2007; Borcka et al., 2008a,b; Matyukhin, 2008; Petrović et al., 2008a,b; Zheng et al., 2008a,b; Petrović et al., 2009). The main objective of most of those studies was to investigate the possibility of guiding ion beams with nanotubes. Biryukov and Bellucci (Biryukov & Bellucci, 2002) looked for the nanotube diameter optimal for channeling high energy ion beams. Krasheninnikov and Nordlund (Krasheninnikov & Nordlund, 2005) studied the channeling of low energy Ar^+ ions through achiral and chiral nanotubes. Petrović et al. (Petrović et al., 2005a) demonstrated that the rainbow effect could play an important role in ion channeling through nanotubes.

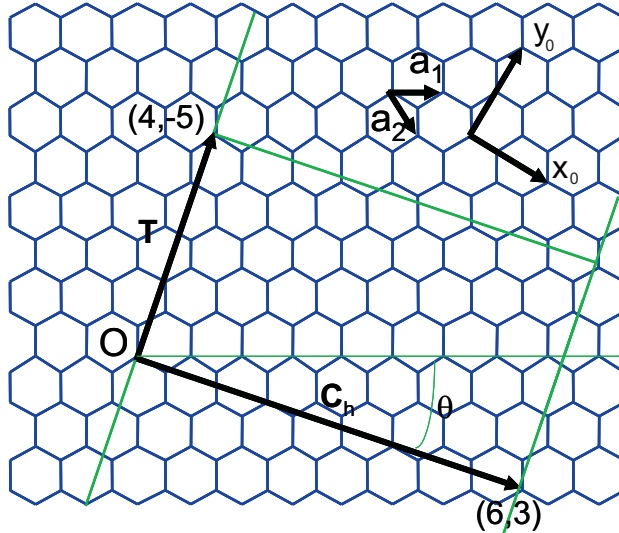


Figure 1: The hexagonal crystal lattice: x_0 and y_0 are the axes of the local reference frame, and \vec{a}_1 and \vec{a}_2 the unit vectors of the lattice. When carbon atoms are placed at the lattice sites, a sheet of carbon atoms is obtained. When rolled up into a cylinder, the sheet of carbon atoms becomes a carbon nanotube: \vec{C}_h is the chiral vector of the nanotube, $\vec{\Theta}_h$ the chiral angle of the nanotube, and \vec{T} the translational vector of the nanotube, which is perpendicular to \vec{C}_h and extends from its origin (point O) to the first lattice point. Rectangle defined by \vec{C}_h and \vec{T} is a unit cell of the nanotube. In the displayed case $\vec{C}_h = (6,3)$ and $\vec{T} = (4,-5)$.

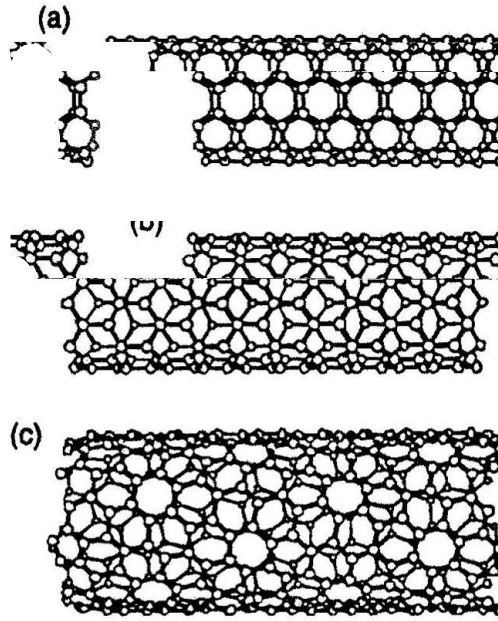


Figure 2: The classification of carbon nanotubes: (a) an armchair nanotube, (b) a zigzag nanotube, and (c) a chiral nanotubes.

The experimental studying of ion channeling through carbon nanotubes is in the initial phase. The most challenging task in such experiments still is to solve the problems of ordering, straightening and holding nanotubes. The first experimental data on ion channeling through nanotubes were reported by Zhu et al. (Zhu et al., 2005). They were obtained with He^+ ions of the kinetic energy of 2 MeV and an array of the well-ordered multi-wall nanotubes grown in a porous anodic aluminum oxide (Al_2O_3) membrane. The authors measured and compared the yields of ions transmitted through the bare Al_2O_3 sample and the Al_2O_3 sample including the nanotubes. The first experiment with electrons and nanotubes was performed by Chai et al. (Chai et al., 2007). They used the 300 keV electrons and studied their transport through the multi-wall nanotubes of the length in the range of 0.7-3.0 μm embedded in a carbon fiber coating. The misalignment of the nanotubes was below 1° . Berdinsky et al. (Berdinsky et al., 2008) succeeded in growing the single-wall nanotubes in the etched ion tracks in a silicon oxide (SiO_2) layer on a silicon substrate. This result has opened a possibility for conducting precise measurements of ion channeling through nanotubes in

a wide ion energy range.

This chapter is devoted to our theoretical studies of proton channeling through carbon nanotubes. We shall first describe briefly the process of ion channeling. Then, the crystal rainbow effect will be introduced, and the theory of crystal rainbows will be presented. We shall continue with a description of the effect of zero-degree focusing of protons channeled through nanotubes. Further, the angular distributions and rainbows in proton channeling through nanotubes will be analyzed. We shall focus on the rainbows in transmission of 1 GeV protons through a straight very short bundle of (10, 10) single-wall carbon nanotube, a bent short bundle of (10, 10) nanotubes, and the straight long (11, 9) nanotubes. Also, the influence of the effect of dynamic polarization of the carbon atoms valence electrons on the angular and spatial distributions of protons transmitted through short nanotubes in vacuum and embedded in dielectric media will be investigated. We shall concentrate on the rainbows in transmission of 0.223-2.49 MeV protons through the short (11, 9) nanotubes in vacuum and embedded in SiO_2 , Al_2O_3 and Ni. Besides, we shall report on the donut effect in transmission of 0.223 MeV protons through a short (11, 9) nanotube, which occurs when the initial ion velocity vector is not parallel to the nanotube axis. In addition, we shall explore the channeling star effect in 1 GeV proton channeling through bundles of nanotubes, which appears when the proton beam divergence angle is larger than the critical angle for channeling.

2 Ion channeling

An axial crystal channel is a part of a crystal in between its neighboring atomic strings being parallel to one of its crystallographic axes. The process of ion motion through the axial crystal channel, in which the angle of its velocity vector relative to the channel axis remains small, is called axial ion channeling (Robinson and Oen, 1963; Lindhard, 1965; Gemmell, 1974). This process is explained by the ion repulsions from the atomic strings defining the channel, which are the results of the series of its correlated collisions with the atoms of the strings. Analogously, a planar crystal channel is a part of the crystal in between its neighboring atomic planes being parallel to one of its crystallographic planes. The process of ion motion through the planar crystal channel is called planar ion channeling (Robinson and Oen, 1963; Lindhard, 1965; Gemmell, 1974).

Theoretical studies of ion channeling through crystals have been going on along two major lines. The first line was founded by Lindhard (Lindhard, 1965) and the second one by Barrett (Barrett, 1971). The Lindhard's approach was analytical and it was developed by the methods of statistical mechanics. He included the continuum approximation, i.e., neglected the longitudinal correlations between the positions of the atoms of one atomic string, did not take into account the transverse correlations between the positions of the atomic strings, and included the assumption of statistical equilibrium in the transverse position plane. The Barrett's approach was via the ion-atom scattering theory and it was numerical. He developed a very realistic computer code for the three-dimensional following of ion trajectories through crystal channels, in which the three approximations used by Lindhard were avoided. The Barrett's approach is more complex, but a number of calculations have shown that it is much more accurate than the Lindhard's approach.

The results that will be presented here have been obtained by a realistic computer code based on the numerical solution of the ion equations of motion through crystal channels. The continuum approximation is included. Consequently, one has to solve only the ion equations of motion in the transverse position plane. The transverse correlations between the positions of the atomic strings are taken into account.

Let us take that the z axis of the reference frame coincides with the channel axis and that its origin lies in the entrance plane of the crystal. The x and y axes of the reference frame are the vertical and horizontal axes, respectively. It is assumed that the interaction of the ion and crystal can be treated classically (Lindhard, 1965; Gemmell, 1974; Barrett, 1971). The interaction of the ion and a crystal's atom is described by an approximation of the Thomas-Fermi interaction potential or any other appropriate interaction potential $-V(r')$, where r' is the distance between the ion and crystal's atom. As a result, we obtain the ion-crystal continuum interaction potential,

$$U(x, y) = \sum_{j=1}^J U_j(x, y), \quad (1)$$

where

$$U_j(x, y) = \frac{1}{d} \int_{-\infty}^{+\infty} V(\rho_j^2 + z^2)^{\frac{1}{2}} dz, \quad (2)$$

is the continuum interaction potential of the ion and the j^{th} atomic string,

$$\rho_j = [(x - x_j)^2 + (y - y_j)^2]^{1/2}, \quad (3)$$

is the distance between the ion and this atomic string, and x and y are the transverse components of the proton position vector; J is the number of atomic strings and d the distance between the atoms of an atomic string.

The thermal vibrations of the crystal's atoms can be taken into account. This is done by averaging $U(x, y)$ over the transverse displacements of the crystal's atoms from their equilibrium positions (Appleton et al., 1967; Nešković, 1986). As a result, one has to substitute $U_j(x, y)$ in Eq. (2) with

$$U_j^{\text{th}}(x, y) = U_j(x, y) + \frac{\sigma_{\text{th}}^2}{2} [\partial_{xx} U_j(x, y) + \partial_{yy} U_j(x, y)], \quad (4)$$

where σ_{th} is the one-dimensional thermal vibration amplitude of the crystal's atoms. Thus, $U^{\text{th}}(x, y)$ is obtained instead of $U(x, y)$.

We neglect the nuclear ion energy loss, i.e., the energy loss resulting from its collisions with the crystal's nuclei. But, the electronic ion energy loss and dispersion of its transmission angle, which are caused by its collisions with the crystal's electrons, can be included. For the specific ion energy loss we use expression

$$-\frac{dE}{dz} = \frac{4\pi Z_1^2 e^4}{m_e v^2} n_e \left(\ln \frac{2m_e \gamma^2 v(z)^2}{\hbar \omega_e} - \beta^2 \right), \quad (5)$$

where Z_1 is the atomic number of the ion, e the elementary charge, m_e the electron mass, $v(z)$ the magnitude of the ion velocity vector, $\beta = v(z)/c$, c the speed of light, $\gamma^2 = (1 - \beta^2)^{-1}$, $n_e = (\partial_{xx} + \partial_{yy})U^{\text{th}}(x, y)/4\pi$ the average of the density of the crystal's electron gas along the z axis, \hbar the reduced Planck constant, and $\omega_e = (4\pi e^2 n_e / m_e)^{\frac{1}{2}}$ the angular frequency of the ion induced oscillations of the crystal's electron gas (Gemmell, 1974; Petrović et al., 2002). For the specific change of the dispersion of the ion transmission angle we use expression

$$\frac{d\Omega_e^2}{dz} = \frac{m_e}{m^2 v^2(z)} \left(-\frac{dE_e}{dz} \right), \quad (6)$$

where $m = m_0\gamma$ is the relativistic ion mass and m_0 the ion rest mass (Gemmell, 1974; Petrović et al., 2002). This dispersion is a measure of the uncertainty of the ion transmission angle. The dispersions of the vertical and horizontal components of the ion transmission angle, Θ_x and Θ_y , are $d\Omega_{ex}^2 = d\Omega_e^2/2$ and $d\Omega_{ey}^2 = d\Omega_e^2/2$, respectively.

The ion equations of motion in the transverse position plane are

$$m \frac{d^2x}{dt^2} = -\partial_x U^{th}(x, y) \quad (7)$$

and

$$m \frac{d^2y}{dt^2} = -\partial_y U^{th}(x, y), \quad (8)$$

where t denotes the time. They are solved by the Runge-Kutta method of the fourth order (Press et al., 1993). In the calculation the time step is chosen in such a way to obtain the fixed longitudinal distance step with the desired accuracy.

At the end of each time step of the calculation the magnitude of the ion velocity vector is corrected using the value of the ion energy loss during the step. The vertical and horizontal components of the ion transmission angle at the end of each time step are chosen within the Gaussian distribution functions defined by Θ_x and $d\Omega_{ex}^2$ and by Θ_y and $d\Omega_{ey}^2$, respectively. The (relativistic) ion mass at the end of each time step is calculated using the corrected value of the magnitude of the ion velocity vector.

The initial direction of the ion velocity vector is defined by the angles its vertical and horizontal components make with the x and y axes, Θ_{x0} and Θ_{y0} , respectively. However, if this direction is uncertain, with the dispersions of Θ_{x0} and Θ_{y0} being $\Omega_{dx}^2 = \Omega_d^2/2$ and $\Omega_{dy}^2 = \Omega_d^2/2$, respectively, where Ω_d is the divergence angle of the initial ion beam, the vertical and horizontal components of the initial ion velocity vector are chosen via the Gaussian distribution functions defined by Θ_{x0} and Ω_{dx}^2 and by Θ_{y0} and Ω_{dy}^2 , respectively.

3 Crystal rainbows

Let us now examine the process of ion transmission through an axial crystal channel. The scheme of the process is given in Figure 3. It is well-known that the motion of an ion close to the channel axis can be treated as an oscillatory

motion around the axis. If the ion impact parameter vector and the angle between its initial velocity vector and the channel axis are fixed, the number of oscillations the ion makes before leaving the crystal depends on its initial kinetic energy. If this energy is sufficiently high for the ion to make less than about a quarter of an oscillation around the channel axis, its trajectory can be approximated by a straight line. If this is true for the majority of ions, one says that the crystal is very thin. If, however, the majority of ions make between about a quarter of an oscillation and about one oscillation, the crystal is thin. The crystal is thick if the majority of ions make more than about one oscillation. Finally, if the majority of ions make much more than one oscillation, the crystal is very thick.

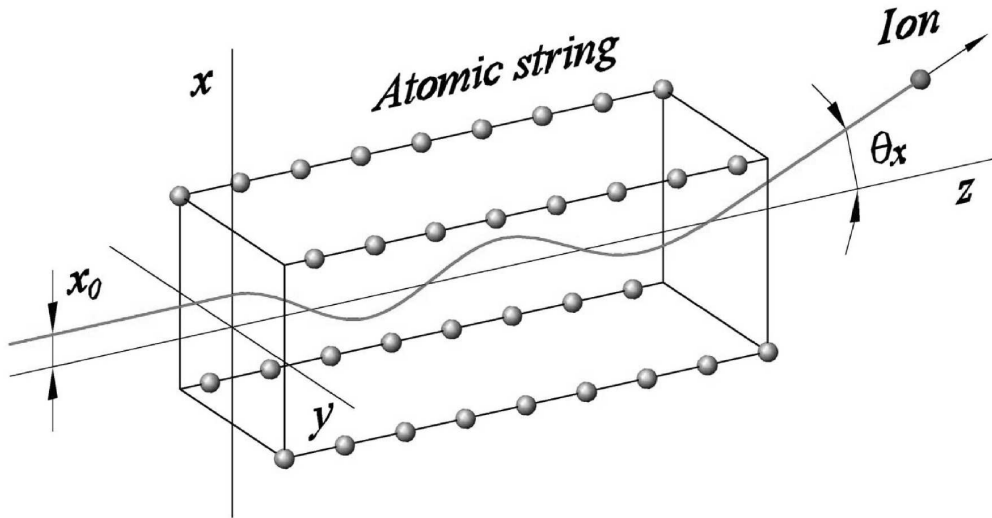


Figure 3: A scheme of the process of ion transmission through an axial crystal channel. The z axis of the reference frame coincides with the channel axis and its origin lies in the entrance plane of the crystal. The x and y axes are the vertical and horizontal axes, respectively. In this example the channel is defined by four atomic strings of the crystal, the initial ion velocity vector lies in the xz plane and it is parallel to the z axis. The vertical components of the ion impact parameter vector and transmission angle are designated by x and Θ_x , respectively. The horizontal components of these variables, y and Θ_y , respectively, are equal to zero.

3.1 Discovery of crystal rainbows

Nešković (Nešković, 1986) showed theoretically that in the ion transmission through an axial channel of a very thin crystal the rainbow occurred, i.e., the ion differential transmission cross section could be singular. His approach was via the ion-molecule scattering theory. In the created model the continuum approximation was included implicitly, the correlations between the positions of the atomic strings of the crystal were included, and the assumption of statistical equilibrium in the transverse position plane was avoided. The effect was observed experimentally for the first time by Krause et al. (Krause et al., 1986). It was named the crystal rainbow effect (Nešković et al., 1993).

The first measurement of crystal rainbows was performed with 7 MeV protons and the $\langle 100 \rangle$ and $\langle 110 \rangle$ Si very thin crystals (Krause et al., 1986). The obtained angular distributions of channeled protons were reproduced using the model of Nešković (Nešković, 1986) with the Lindhard's proton-crystal continuum interaction potential (Lindhard, 1965). Krause et al. have also performed the high resolution measurements of the angular distributions of 2-9 MeV protons and 6-30 MeV C^{4+} , C^{5+} and C^{6+} ions transmitted through the $\langle 100 \rangle$ Si thin crystal (Krause et al., 1994). The interpretation of the obtained results was done using the computer code of Barrett (Barrett, 1971) with the Molière's ion-crystal continuum interaction potential. Those measurements demonstrated clearly the possibilities of using crystal rainbows for exploring the properties of thin crystals, e.g., for precise local measurement of their thickness, with the accuracy of a few atomic layers, and for precise differential measurement of the electron density and ion energy loss within their channels (Nešković & Petrović, 2003).

As it has been said in part §1 of this chapter, Petrović et al. (Petrović et al., 2005a) showed theoretically that the rainbow effect can also appear with carbon nanotubes. This will be discussed in detail in part §5 of this chapter.

3.2 Theory of crystal rainbows

Krause et al. (Krause et al., 1986) and Miletić et al. (Miletić et al., 1996, 1997) investigated the periodicity of evolution of the angular distribution of channeled ions with the reduced crystal thickness, which is

$$\Lambda = \frac{f(q, m)L}{v_0}, \quad (9)$$

where $q = Z_1 e$, m and v_0 are the ion charge, mass and magnitude of the initial ion velocity vector, respectively, L is the crystal thickness, and $f(q, m)$ is the average frequency of the ion motion close to the channel axis. They found that the evolution of the angular distribution of channeled ions could be divided into cycles. The first cycle lasts for Λ between 0 and 0.5, the second cycle for Λ between 0.5 and 1, and so on. These cycles were named the rainbow cycles. We note that the crystal is very thin if Λ is smaller than ~ 0.25 , it is thin if Λ is between ~ 0.25 and ~ 1 , it is thick if Λ is larger than ~ 1 , and it is very thick if Λ is much larger than ~ 1 . For $\Lambda = (n - 1)/2 + 1/4$, where $n = 1, 2, \dots$ is the order of the rainbow cycle, a large part of the ion beam is focused around the origin in the transverse position plane. This is an effect of spatial focusing, which is called the effect superfocusing of channeled ions Demkov & Meyer (2004); Nešković et al. (2009). For $\Lambda = n/2$, with $n = 1, 2, \dots$, a large part of the ion beam is parallel to the channel axis, i.e., it is focused around the origin in the transmission angle plane. This is an effect of angular focusing, which is called the effect of zero-degree focusing of channeled ions (Miletić et al., 1996, 1997).

In order to describe the ion transmission through axial channels of crystals that are not necessarily very thin, Petrović et al. (Petrović et al., 2000) generalized the model of Nešković (Nešković, 1986) and formulated the theory of crystal rainbows. Let us describe this theory briefly. We take that the z axis of the reference frame coincides with the channel axis and its origin lies in the entrance plane of the crystal. The x and y axes of the reference frame are the vertical and horizontal axes, respectively. This is shown in Fig. 3. It is assumed that the interaction of the ion and crystal can be treated classically (Lindhard, 1965). The interaction of the ion and a crystal's atom is described by the Lindhard's (Lindhard, 1965) or Molière's approximation (Molière, 1947) of the Thomas-Fermi interaction potential, or any other appropriate interaction potential. We apply the continuum approximation, i.e., the atomic strings are treated as if they are continual, rather than discrete (Lindhard, 1965). As a result, we obtain the Lindhard's or Molière's ion-crystal continuum interaction potential, or another appropriate continuum interaction potential. The thermal vibrations of the crystal's atoms can be taken into account as it is described in part 2 of this chapter (Appleton et al., 1967). We neglect the nuclear ion energy loss, i.e., the energy loss resulting from its collisions with the crystal's nuclei. But, the electronic ion energy loss and dispersion of its transmission angle, which are caused by its collisions with the crystal's electrons, can be included as it is described in part 2 of

this chapter (Gemmell, 1974; Petrović et al., 2002).

The transverse components of the initial ion position vector are equal to the components of its impact parameter vector, x_0 and y_0 , while the transverse components of the initial ion velocity vector are v_{x0} and v_{y0} . In order to obtain the components of the final ion position and velocity vectors, one must solve the ion equations of motion. Since we apply the continuum approximation and the electronic ion energy loss during the whole transmission process remains small, we assume that the longitudinal ion motion is uniform and solve only the ion equations of motion in the transverse position plane. In order to compensate the inaccuracies resulting from this assumption, the magnitude of the ion velocity vector at the end of each step of the calculation is corrected using the value of the ion energy loss during the step. We also correct the direction of the ion velocity vector at the end of each step of the calculation using the value of the change of the dispersion of its transmission angle during the step. This is how the ion energy loss and change of the dispersion of its transmission angle are included in the calculations. The relativistic effect is taken into account by changing the ion mass at the end of each step of the calculation using the corrected value of the magnitude of the ion velocity vector. The obtained transverse components of the final ion position vector are $x(x_0, y_0, \Lambda)$ and $y(x_0, y_0, \Lambda)$, and the transverse components of the final ion velocity vector are $v_x(x_0, y_0, \Lambda)$ and $v_y(x_0, y_0, \Lambda)$. Since the ion transmission angle during the whole transmission process remains small, the components of the final ion transmission angle are $\Theta_x(x_0, y_0, \Lambda) = v_x/v$ and $\Theta_y(x_0, y_0, \Lambda) = v_y/v$, where $v = v(x_0, y_0, \Lambda)$ is the magnitude of the final ion velocity vector. The spatial and angular distributions of transmitted ions, in the exit plane of the crystal, are generated by the computer simulation method. The spatial and angular distributions of ions in the entrance plane of the crystal are determined by the spatial and angular characteristics of the chosen initial ion beam. If the ion, during its motion along the channel, enters any of the cylindrical regions around the atomic strings of the radius equal to the screening radius of a crystal's atom, it is excluded from the calculations.

Since the ion transmission angle during the whole transmission process remains small, the ion differential transmission cross section is

$$\sigma(x_0, y_0, \Lambda) = \frac{1}{|J_{\Theta}(x_0, y_0, \Lambda)|}, \quad (10)$$

where

$$J_{\Theta}(x_0, y_0, \Lambda) = \partial_{x_0} \Theta_x \partial_{y_0} \Theta_y - \partial_{y_0} \Theta_x \partial_{x_0} \Theta_y \quad (11)$$

is the Jacobian of the components of its transmission angle, which equals the ratio of the infinitesimal surfaces in the transmission angle plane and impact parameter plane. It describes the mapping of the impact parameter plane to the transmission angle plane. Hence, equation $J_{\Theta}(x_0, y_0, \Lambda) = 0$ gives the angular rainbow lines in the impact parameter plane, along which the mapping is singular. The images of these lines determined by functions $\Theta_x(x_0, y_0, \Lambda)$ and $\Theta_y(x_0, y_0, \Lambda)$ are the rainbow lines in the transmission angle plane.

On the other hand, the mapping of the impact parameter plane to the transverse position plane is described by the Jacobian of the transverse components of the ion position vector. This Jacobian, which equals the ratio of the infinitesimal surfaces in the transverse position plane and impact parameter plane, reads

$$J_{\rho}(x_0, y_0, \Lambda) = \partial_{x_0} x \partial_{y_0} y - \partial_{y_0} x \partial_{x_0} y. \quad (12)$$

Thus, equation $J_{\rho}(x_0, y_0, \Lambda) = 0$ gives the spatial rainbow lines in the impact parameter plane, along which the mapping is singular. The images of these lines determined by functions $x(x_0, y_0, \Lambda)$ and $y(x_0, y_0, \Lambda)$ are the rainbow lines in the transverse position plane.

The rainbow lines in the transverse position plane and transmission angle plane separate the bright and dark regions in these planes. Their shapes are classified by catastrophe theory (Thom, 1975; Nešković & Perović, 1987; Nešković et al., 1993). Hence, one says that the ion beam dynamics in the channel has the catastrophic character.

4 Zero-degree focusing of protons channeled through bundles of nanotubes

The first calculations of the effect of zero-degree focusing of channeled ions, which is defined in part §3.2 of this chapter, were performed by Miletić et al. (Miletić et al., 1996, 1997). In the former study the projectiles were 25 MeV C^{6+} ions and the target was the $\langle 100 \rangle$ Si crystal of the thickness between 0 and 2.7 μm , while in the latter study the projectiles were Ne^{10+} ions of the

kinetic energies between 1 and 37 MeV while the target was the 1.0 μm thick $\langle 100 \rangle$ Si crystal. The effect has not yet been observed experimentally.

We shall describe here the effect of zero-degree focusing of 1 GeV protons channeled through the (10, 10) single-wall carbon nanotubes (Nešković et al., 2005; Petrović et al., 2005b). Such a nanotube is achiral, i.e., its atomic strings are parallel to its axis. It is assumed that the nanotubes form a bundle whose transverse cross-section can be described via a (two-dimensional) hexagonal or rhombic superlattice with one nanotube per primitive cell (Thess et al., 1996). We choose the z axis of the reference frame to coincide with the bundle axis and its origin to lie in the entrance plane of the bundle. The arrangement of the nanotubes is such that their axes intersect the x and y axes of the reference frame, which are the vertical and horizontal axes, respectively (Petrović et al., 2005a). We take into account the contributions of the nanotubes lying on the two nearest rhombic coordination lines, relative to the center of the primitive cell of the (rhombic) superlattice.

The calculations are performed using the theory of crystal rainbows, which is described in part §3.2 of this chapter. The interaction of the proton and a nanotube atom is described by the Molière's approximation (Molière, 1947) of the Thomas-Fermi interaction potential, which reads

$$V(r') = \frac{Z_1 Z_2 e^2}{r'} [0.35 \exp(-0.3r'/a) + 0.55 \exp(-1.2r'/a) + 0.10 \exp(-6.0r'/a)] \quad (13)$$

where $Z_1 = 1$ and $Z_2 = 6$ are the atomic numbers of the proton and nanotube atom, respectively, e is the elementary charge, r' is the distance between the proton and nanotube atom, $b = 0.3/a$, $a = [9\pi^2/(128Z_2)]^{\frac{1}{3}} a_0$ is the screening radius of the nanotube atom, and a_0 is the Bohr radius. It has been proven that this expression provides excellent agreement with experimental results in the field of ion channeling (Krause et al., 1994). The application of the continuum approximation gives the Molière's proton-bundle continuum interaction potential, which reads

$$U(x, y) = \sum_{i=1}^I \sum_{j=1}^J U_{ij}(x, y), \quad (14)$$

where

$$U_{ij}(x, y) = \frac{2Z_1Z_2e^2}{d} [0.35K_0(0.3\rho_{ij}/a) + 0.55K_0(1.2\rho_{ij}/a) + 0.10K_0(6.0\rho_{ij}/a)] \quad (15)$$

is the Molière's continuum interaction potential of the proton and the j th atomic string of the i^{th} nanotube within the bundle,

$$\rho_{ij} = [(x - x_{ij})^2 + (y - y_{ij})^2]^{\frac{1}{2}} \quad (16)$$

is the distance between the proton and this atomic string, and x and y are the transverse components of the proton position vector; $I = 16$ is the number of nanotubes within the bundle, $J = 40$ is the number of atomic strings of a nanotube, $d = 0.24$ nm is the distance between the atoms of an atomic string, and K_0 denotes the modified Bessel function of the second kind and 0^{th} order. This means that the number of atomic strings within the bundle is $I \times J = 640$. The thermal vibrations of the nanotube atoms are taken into account. This is done by substituting $U_{ij}(x, y)$ in Eq. (14) with

$$U_{ij}^{th}(x, y) = U_{ij}(x, y) + \frac{\sigma_{th}^2}{2} [\partial_{xx}U_{ij}(x, y) + \partial_{yy}U_{ij}(x, y)], \quad (17)$$

where $\sigma_{th} = 5.3$ pm is the one-dimensional thermal vibration amplitude of the nanotube atoms (Hone et al., 2000). Thus, $U^{th}(x, y)$ is obtained instead of $U(x, y)$. The electronic proton energy loss and dispersion of its transmission angle, caused by its collisions with the nanotube electrons, are neglected. The nanotube radius is 0.67 nm (Saito et al., 2001) and the distance between the axes of two neighboring nanotubes is 1.70 nm (Thess et al., 1996). The components of the proton impact parameter vector are chosen uniformly within the primitive cell of the (rhombic) superlattice. The initial proton velocity vectors are all taken to be parallel to the bundle axis.

The nanotube walls define two separate regions in the transverse position plane: inside the nanotubes and in between them (Petrović et al., 2005a). Accordingly, the bundle contains two types of channels: the circular one, whose center coincides with the center of the region inside each nanotube, and the triangular one, whose center coincides with the center of the region in between each three neighboring nanotubes. It is clear that in this case one has to define two average frequencies of the proton motion close to the channel axis, corresponding to the protons moving close to the centers of the circular and triangular channels. The two frequencies can be determined

from the second order terms of the Taylor expansions of the proton-bundle continuum interaction potential in the vicinities of the centers of the two types of channels. Consequently, there are two reduced bundle lengths, Λ_1 and Λ_2 , corresponding to the proton motions close to the axes of the circular and triangular channels, respectively.

Figure 4(a) shows the dependence of the zero-degree yield of protons propagating along the circular channels of the bundle on the bundle length, L , in the range of 0-200 μm ; the Λ_1 axis is shown too. For the region in the transmission angle plane in the vicinity of its origin we take the region in which the proton transmission angle, $\Theta = (\Theta_x^2 + \Theta_y^2)^{\frac{1}{2}}$, where Θ_x and Θ_y are its vertical and horizontal components, respectively, is smaller than 0.0109 mrad. The initial number of protons is 174 976. The six maxima of the dependence correspond to the ends of the first six rainbow cycles, where the proton beam channeled through the circular channels is quasi-parallel (Miletić et al., 1996, 1997). The positions of these maxima should be close to $\Lambda_1 = 0.5, 1, 1.5, \dots$. However, this is not true. For example, the position of the first maximum of the dependence is $\Lambda_1 = 0.35$. The large deviations of the values of these position from their expected values are explained by the strong anharmonicity of the proton-bundle continuum interaction potential in the vicinities of the centers of the circular channels (Miletić et al., 1997).

The dependence of the zero-degree yield of protons propagating along the triangular channels of the bundle on L in the range of 0-200 μm is given in Fig. 4(b); the Λ_2 axis is shown too. The initial number of protons is 136 658. The dependence has 27 maxima, and they correspond to the ends of the first 27 rainbow cycles, where the proton beam channeled through the triangular channels is quasi-parallel (Miletić et al., 1996, 1997). The positions of these maxima are close to $\Lambda_2 = 0.5, 1, 1.5, \dots$. For example, the position of the first maximum of the dependence is $\Lambda_2 = 0.49$. The small deviations of the values of these position from their expected values are attributed to the weak anharmonicity of the proton-bundle continuum interaction potential in the vicinities of the centers of the triangular channels (Miletić et al., 1997). It should be noted that the total zero-degree yield of channeled protons, i.e., of protons channeled through both the circular and triangular channels, as a function of L is the sum of the zero-degree yields shown in Fig. 4(a) and Fig. 4(b).

We have also investigated the effect of zero-degree focusing of 1 GeV protons channeled through the (10, 0) single-wall carbon nanotubes (Borka et al., 2008). The study has been performed in the same way as in the case of (10,

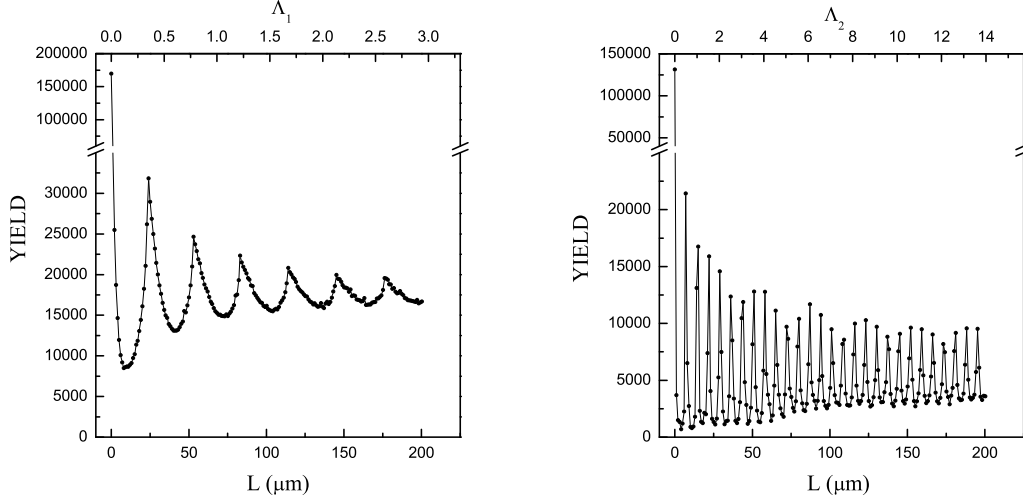


Figure 4: (a) The zero-degree yield of 1 GeV protons channeled through the circular channels of the bundle of (10, 10) single-wall carbon nanotubes as a function of the bundle length, L . (b) The zero-degree yield of 1 GeV protons channeled through the triangular channels of the bundle of (10, 10) single-wall carbon nanotubes as a function of the bundle length, L .

10) nanotubes. The number of nanotubes within the bundle is $I = 16$, the number of atomic strings of a nanotube is $J = 20$, the distance between the atoms of an atomic string is $d = 0.21$ nm. The nanotube radius is 0.39 nm (Saito et al., 2001), and the distance between the axes of two neighboring nanotubes is 1.10 nm (Zhang et al., 2003). In this case the dependence of the zero-degree yield of protons channeled through the circular channels of the bundle on L in the range of 0-200 μm contains 26 maxima. The positions of these maxima are close to $\Lambda_1 = 0.5, 1, 1.5, \dots$. The average distance between the maxima is $\Delta\Lambda_1 = 0.49$. This means that the anharmonicity of the proton-bundle continuum interaction potential in the vicinities of the centers of the circular channels is weak (Miletić et al., 1997). In this case the dependence of the zero-degree yield of protons channeled through the triangular channels of the bundle on L in the range of 0-200 μm contains 37 maxima. The positions of these maxima are very close to $\Lambda_2 = 0.5, 1, 1.5, \dots$. The average distance between the maxima is $\Delta\Lambda_2 = 0.50$. Thus, one can say that the anharmonicity of the proton-bundle continuum interaction potential in the vicinities of the centers of the triangular channels is very

weak (Miletić et al., 1997).

The comparison of the zero-degree yields of protons channeled through the circular and triangular channels of the bundles as functions of L in the cases of (10, 10) and (10, 0) nanotubes shows that:

- (i) when the circular channels are considered, the average frequency of the proton motion close to the channel axis is much lower in the former than in the latter case,
- (ii) when the triangular channels are considered, the average frequency of the proton motion close to the channel axis is lower in the former than in the latter case, and
- (iii) when the circular and triangular channels are compared to each other, the ratio of the average frequencies of the proton motions close to the channel axes in the circular and triangular channels is much smaller in the former than in the latter case.

Thus, one can conclude that the measurements of the effect of zero-degree focusing of channeled protons can give the information on the transverse lattice structures of the nanotubes and of the bundles.

5 Angular distributions and rainbows in proton channeling through nanotubes

We shall present in this part of the chapter the angular distributions and rainbows in channeling 1 GeV protons through a straight very short bundle of (10, 10) single-wall carbon nanotubes (Petrović et al., 2005a), a bent short bundle of (10, 10) nanotubes (Nešković et al., 2005), and the straight long (11, 9) nanotubes (Petrović et al., 2008b).

5.1 Rainbows with a straight very short bundle of nanotubes

The system we investigate here is a 1 GeV proton moving through a bundle of (10, 10) single-wall carbon nanotubes that is described in part 4 of this chapter. The bundle length is 1 μm (Petrović et al., 2005a). The reduced

bundle lengths corresponding to the proton channeling inside the nanotubes and in between them, i.e., through the circular and triangular channels of the bundle, are $\Lambda_1 = 0.015$ and $\Lambda_2 = 0.070$, respectively. These values tell us that in both cases the majority of protons make before leaving the bundle less than a quarter of an oscillation around the channel axis ($\Lambda_1, \Lambda_2 < 0.25$). Therefore, one can say that the bundle we investigate is very short.

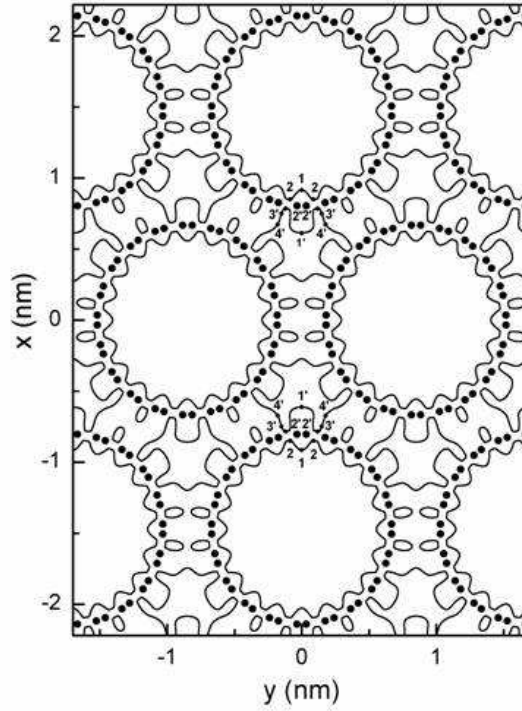


Figure 5: The rainbow lines in the impact parameter plane for 1 GeV protons transmitted through the $1 \mu\text{m}$ long (10, 10) single-wall carbon nanotubes.

The calculations are performed using the theory of crystal rainbows, which is described in part §3.2 of this chapter. The interaction of the proton and bundle is described by Eqs. (14)-(16). We take into account the effect of thermal vibrations of the nanotube atoms, and this is done by Eq. (17).

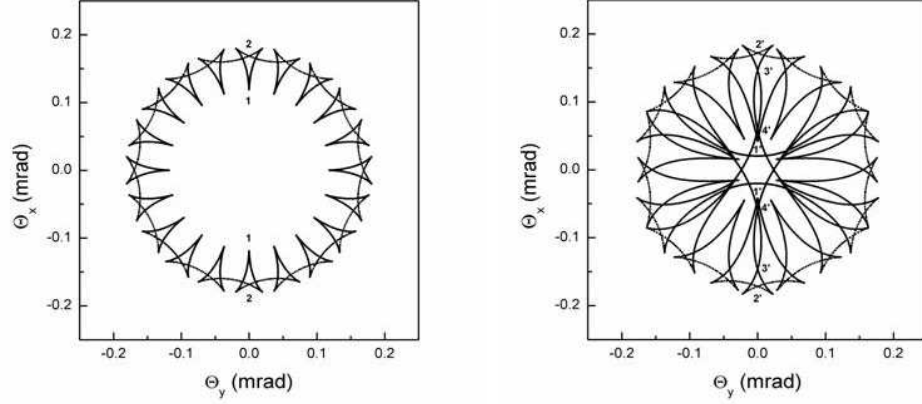


Figure 6: The rainbow lines in the transmission angle plane corresponding to the rainbow lines in the impact parameter plane (shown in Fig. 1) lying (a) inside each nanotube, and (b) in between each four neighboring nanotubes.

However, the electronic proton energy loss and dispersion of its transmission angle are neglected. This is justified by the fact that the bundle is very short. If the bundle were long ($\Lambda_1, \Lambda_2 > 1$), these effect would cause the smearing out of the angular distributions of channeled protons (Petrović et al., 2002).

Figure 5 shows the rainbow lines in the impact parameter plane in the case under consideration. One can see that inside each nanotube, i.e., inside each circular channel of the bundle, there is one (closed) rainbow line, while in between each three neighboring nanotubes, i.e., inside each triangular channel of the bundle, there are one larger and four smaller (closed) rainbow lines.

The rainbow line in the transmission angle plane that is the image of the rainbow line in the impact parameter plane lying inside each nanotube is shown in Figure 6(a). It consists of 20 connected cusped triangular lines lying along the lines $\varphi = \tan^{-1}(\Theta_y/\Theta_x) = 2(n+1)\pi/20$, $n = 0-19$, which correspond to the parts of the rainbow line in the impact parameter plane in front of the 20 pairs of atomic strings defining the nanotube (see Fig. 5). Points 1 and 2 are the intersection points of the rainbow line in the transmission angle plane with the line $\Theta_y = 0$. Points 1 are the apices of the cusps and points 2 are the intersections of the parts of the rainbow line. The corresponding points in the impact parameter plane are also designated by

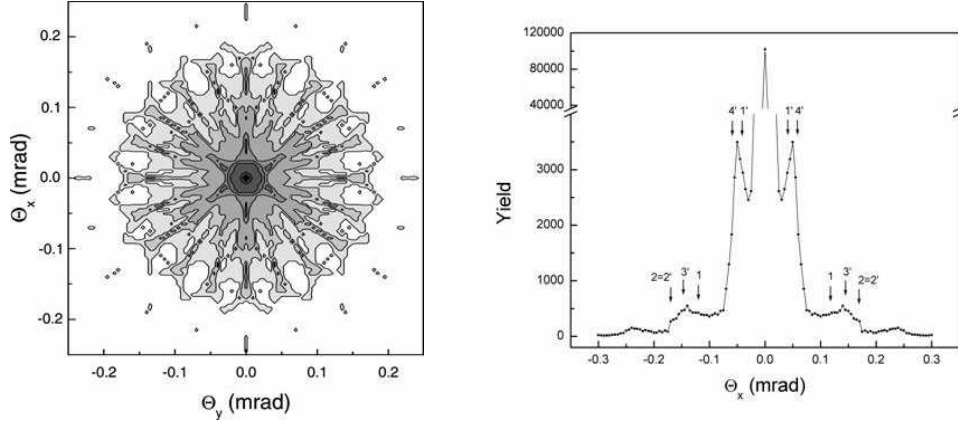


Figure 7: (a) The angular distribution of 1 GeV protons transmitted through the $1 \mu\text{m}$ long bundle of (10, 10) single-wall carbon nanotubes. The areas in which the yields of transmitted protons are larger than 0.13, 0.26, 0.39, 1.3, 2.6, 3.9, 13, 26, 39 % of the maximal yield are designated by the increasing tones of gray color. (b) The corresponding yield of transmitted protons along the line $\Theta_y = 0$.

1 and 2.

Figure 6(b) shows the rainbow lines in the transmission angle plane that are the images of the rainbow lines in the impact parameter plane lying in between each four neighboring nanotubes. The analysis shows that the rainbow pattern consists of two cusped equilateral triangular rainbow lines in the central region of the transmission angle plane with the cusps lying along the lines $\varphi = 2n\pi/3$ and $\varphi = (2n + 1)\pi/3$, $n = 0-2$, each connected with three pairs of cusped triangular rainbow lines lying along the same lines, and eight cusped triangular rainbow lines lying in between the six pairs of triangular lines. The two equilateral triangular lines each connected with the three pairs of triangular lines are the images of the two larger rainbow lines while the eight triangular lines are the images of the eight smaller rainbow lines in the impact parameter plane (see Fig. 5). Points 1', 2', 3' and 4' are the intersection points of the rainbow lines in the scattering angle plane with line $\Theta_y = 0$. Points 1' are the apices of the cusps, and points 2', 3' and 4' are the intersections of the parts of the larger rainbow lines. The corresponding points in the impact parameter plane are also designated by 1', 2', 3' and 4'.

Figure 7(a) shows the angular distribution of transmitted protons. The

number of transmitted protons is 2 142 538. The areas in which the yields of transmitted protons are larger than 0.13, 0.26 and 0.39 %, 1.3, 2.6 and 3.9 %, and 13, 26 and 39 % of the maximal yield are designated by the increasing tones of gray color. At the very low level of the yield, corresponding to the boundary yields of 0.13, 0.26 and 0.39 % of the maximal yield, there are 20 triangular forms in the peripheral region of the transmission angle plane, with the maxima lying on the lines $\varphi = 2(n + 1)\pi/20$, $n = 0-19$. Further, at the low level of the yield, corresponding to the boundary yields of 1.3, 2.6 and 3.9 % of the maximal yield, there is a hexagonal structure in the central region of the transmission angle plane, with the maxima lying on the lines $\varphi = n\pi/3$, $n = 0-5$. Finally, at the high level of the yield, corresponding to the boundary yields of 13, 26 and 39 % of the maximal yield, there is a pronounced maximum at the origin of the transmission angle plane. The analysis shows that the first part of the angular distribution is generated by the protons with the impact parameters close to the atomic strings defining the nanotubes - the 20 triangular forms correspond to the 20 pairs of atomic strings defining the nanotubes. The second part of the angular distribution is generated by the protons with the impact parameters in between the nanotubes but not close to the centers of the triangular channels. The third part of the angular distribution is generated to a larger extent by the protons with the impact parameters close to the centers of the circular channels and to a smaller extent by the protons with the impact parameters close to the centers of the triangular channels. It should be noted that most of the protons that generate the third part of the angular distribution interact with the nanotubes very weakly - they move through the space inside the nanotubes virtually as through a drift space. Thus, we can say that the angular distribution contains the information on the transverse lattice structure of the bundle. Its first part (the peripheral region of the transmission angle plane) provides the information on the individual nanotubes while its second part (the central region of the transmission angle plane) provides the information on the way they are connected to each other.

The comparison of Figs. 6(a) and 6(b) with Fig. 7(a) shows clearly that the shape of the rainbow pattern determines the shape of the angular distribution of transmitted protons. Also, each maximum of the angular distribution, except the maximum lying at the origin of the transmission angle plane, can be attributed to one of the above mentioned characteristic rainbow points in the transmission angle plane. Thus, one can conclude that the rainbow pattern enables the full explanation of the angular distribution.

Figure 7(b) gives the low and very low levels of the yield of transmitted protons along line $\Theta_y = 0$. The arrows indicate the above mentioned characteristic rainbow points in the transmission angle plane. It is evident that the two maxima at the low level of the yield can be explained by points 1' and 4' in the transmission angle plane, and the two shoulders at the very low level of the yield by points 1, 2, 2' and 3'. This means that the characteristic rainbow points in the transmission angle plane can provide the information on the continuum potential of the bundle at the corresponding points in the impact parameter plane, and, hence, on the average electron density in the bundle at these points (see Fig. 5). The two maxima at the low level of the yield can be used to measure the average electron density at points 1' and 4', lying in between the nanotubes, while the two shoulders at the very low level of the yield can be used to measure the average electron density at points 1 and 2, lying in the nanotube, and at points 2' and 3', lying in between the nanotubes. The obtained data can help one compare various theoretical approaches and determine the electron structure of the bundle.

We have also performed the analyses of the angular distributions of 1 GeV protons transmitted through the 1 μm long bundles of (10, 0) and (5, 5) single-wall carbon nanotubes. These nanotubes are achiral too. In the former case each nanotube consists of 20 atomic strings and in the latter case of 10 pairs of atomic strings. The angular distribution in the (10, 0) case is similar to the one in the (10, 10) case while the angular distribution in the (5, 5) case is very different from the one in the (10, 10) case. In both cases it is easy to establish the correspondence between the parts of the angular distributions and the transverse lattice structures of the bundles. It should be also noted that the evolution of the angular distribution in the (10, 0) case (Borka et al., 2005) with the proton energy or the bundle length is different from the evolution in the (10, 10) case (Petrović et al., 2005b), enabling one to distinguish between the two types of bundles. Thus, the obtained results can lead to a new method of characterization of achiral carbon nanotubes, based on the rainbow effect. This method would be complementary to the existing method of characterization of nanotubes by electrons impinging on them transversely rather than longitudinally, which is based on the diffraction effect (see, e.g., Lucas et al. (2002)).

5.2 Rainbows with a bent short bundle of nanotubes

Again, the system we explore is a 1 GeV proton moving through a bundle of (10, 10) single-wall carbon nanotubes that is described in part §4 of this chapter. However, now, the bundle is bent along the y axis. The bundle length is 7 μm and its bending angle is varied in the range of 0-1.5 mrad (Nešković et al., 2005). In this case the critical angle for channeling is $\Psi_C = 0.314$ mrad. If the angle of the proton velocity vector relative to the channel axis is above Ψ_C , the proton is dechanneled. The reduced bundle lengths corresponding to the proton channeling through the circular and triangular channels of the bundle are $\Lambda_1 = 0.103$ and $\Lambda_2 = 0.488$, respectively. Thus, in the circular channels the majority of protons make before leaving the bundle less than a quarter of an oscillation around the channel axis ($\Lambda_1 < 0.25$), and in the triangular channel they make close to half an oscillation ($\Lambda_2 \approx 0.5$). Hence, for the protons in the circular channels the bundle is very short while for those in the triangular channels it is short ($\Lambda_1 < 1$).

The calculations are performed using the theory of crystal rainbows, which is described in part §3.2 of this chapter. The interaction of the proton and bundle is described by Eqs. (14)-(16). We take into account the effect of thermal vibrations of the nanotube atoms, and this is done by Eq. (17). However, the electronic proton energy loss and dispersion of its transmission angle are neglected. This is justified by the above given values of Λ_1 and Λ_2 .

The bundle length has been chosen to correspond to the first maximum of the zero-degree yield of protons propagating along the triangular channels of the bundle as a function of the bundle length, which is given in Fig. 4(b). Thus, the part of the proton beam transmitted through the triangular channels is quasi-parallel, and we can investigate in an easier manner the behavior of the proton beam transmitted through the circular channels.

Figure 5.4(a) shows the angular distribution of protons transmitted through the straight bundle, i.e., for its bending angle $\alpha = 0$. The sizes of a bin along the Θ_x and Θ_y axes are equal to 0.00667 mrad while the initial number of protons is 866 976. The angular distribution contains (i) a pronounced maximum at the origin of the transmission angle plane, (ii) six non-pronounced maxima lying along the lines defined by $\varphi = \tan^{-1}(\Theta_y/\Theta_x) = n\pi/3$, $n = 0-5$, and (iii) a non-pronounced circular part. The rainbow pattern in the transmission angle plane obtained for $\alpha = 0$ is given in Fig. 8(b). It contains (i) two six-cusp lines very close to the origin of the transmission angle plane, corresponding to two complex lines in the impact parameter plane close to

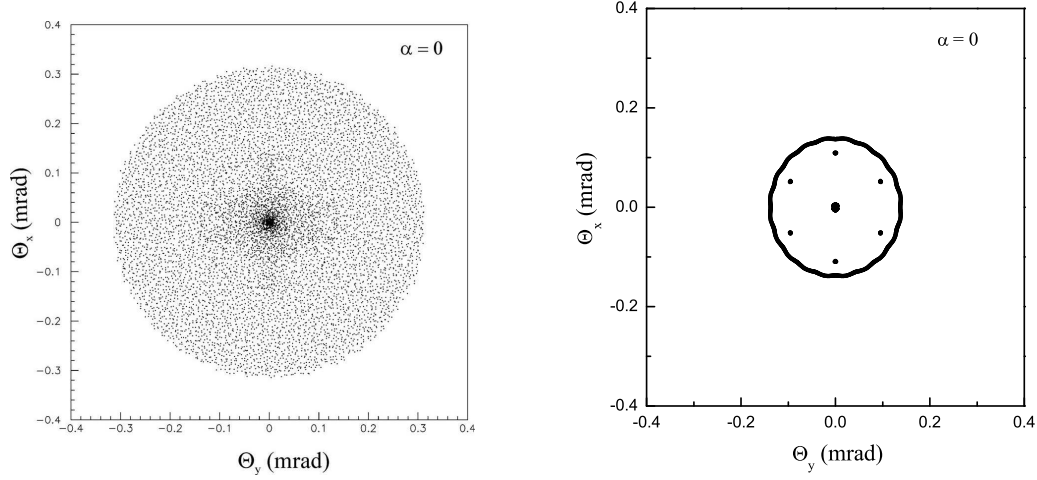


Figure 8: (a) The angular distribution of 1 GeV protons transmitted through the straight bundle of (10, 10) single-wall carbon nanotubes of the length of $L = 7 \mu\text{m}$. (b) The corresponding rainbow pattern in the transmission angle plane.

the centers of the two triangular channels making each rhombic channel of the bundle, (ii) six points lying along the lines defined by $\varphi = n\pi/3$, $n = 0-5$, corresponding to two times three points in the impact parameter plane within the two triangular channels making each rhombic channel, and (iii) a circular line, corresponding to a circular line in the impact parameter plane within each circular channel. The comparison of the results given in Figs. 8(a) and 5.4(b) shows that the angular distribution can be explained as follows: (i) the pronounced maximum at the origin of the transmission angle plane is generated by the protons with the impact parameter vectors close to the centers of each circular channel and each triangular channel, (ii) the six non-pronounced maxima by the protons with the impact parameter vectors close to the six rainbow points (within each rhombic channel), and (iii) the non-pronounced circular part by the protons with the impact parameter vectors close to the circular rainbow line (within each circular channel).

Figure 9(a) shows the angular distribution of protons transmitted through the bundle obtained for $\alpha = 0.2$ mrad. The transmission angle plane is parallel to the exit plane of the bundle. The sizes of a bin along the Θ_x and Θ_y axes and the initial number of protons are the same as in the case of $\alpha = 0$. One can see easily that the angular distribution lies in the region

$\Theta_y > -0.2$ mrad, demonstrating that the proton beam is bent by the bundle effectively. The centrifugal force made the average bending angle of the proton beam smaller than 0.2 mrad. The angular distribution contains (i) a part having the shape of an acorn with two maxima at points (± 0.096 mrad, -0.054 mrad), and (ii) eight additional maxima close and in between the two maxima. The rainbow pattern in the transmission angle plane for $\alpha = 0.2$ mrad is given in Fig. 9(b). It contains (i) an acorn-like line with two joining points of its branches, corresponding to a complex line in the impact parameter plane within each circular channel of the bundle, and (ii) eight groups of points, corresponding to two times four groups of points in the impact parameter plane within the two triangular channels making each rhombic channel. The comparison of the results given in Figs. 9(a) and 9(b) shows that the angular distribution can be explained as follows: (i) the acorn-like part with the two maxima is generated by the protons with the impact parameter vectors close to the acorn-like rainbow line with the two joining points (within each circular channel), and (ii) the eight additional maxima by the protons with the impact parameter vectors close to the eight groups of rainbow points (within each rhombic channel).

Figure 10 gives the dependences of the yields of protons transmitted

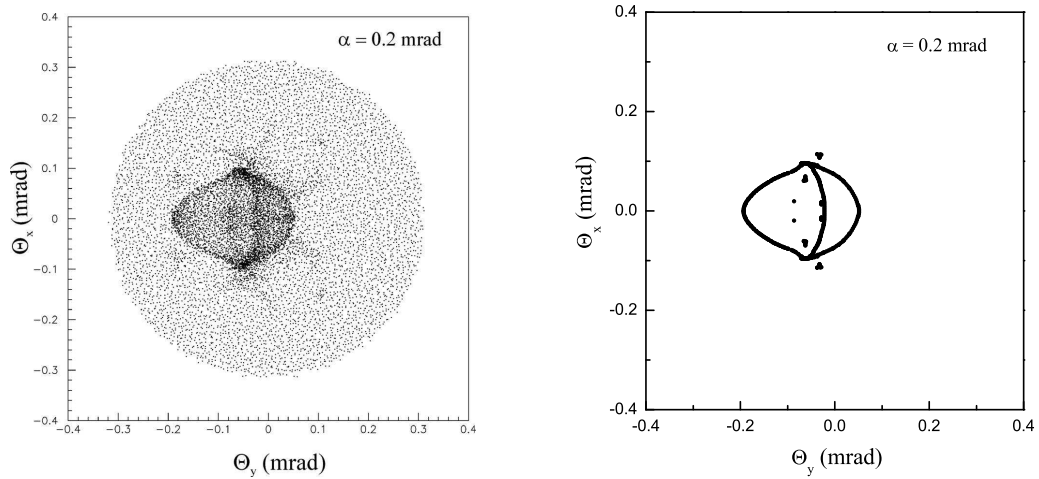


Figure 9: (a) The angular distribution of 1 GeV protons transmitted through the bent bundle of (10, 10) single-wall carbon nanotubes of the length of $L = 7 \mu\text{m}$ for the bending angle $\alpha = 0.2$ mrad. (b) The corresponding rainbow pattern in the transmission angle plane.

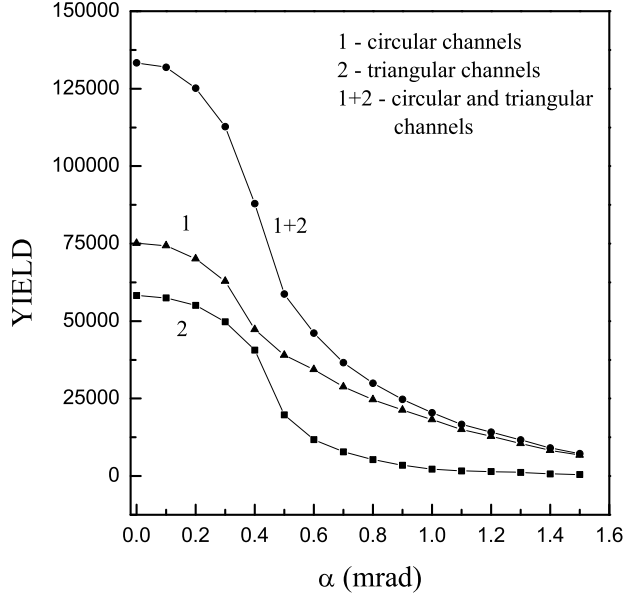


Figure 10: The yields of protons transmitted through the circular channels, the triangular channels, and both the circular and triangular channels of the bent bundle of (10, 10) single-wall carbon nanotubes of the length of $L = 7 \mu\text{m}$ as functions of the bending angle, α .

through the circular channel and the triangular channels of the bundle on α in the range of 0-1.5 mrad. The initial numbers of protons are 77 866 for the former dependence and 60 770 for the latter dependence. The inflection points of the dependences appear at $\alpha = 0.35$ and 0.45 mrad, respectively. These values ought to be compared to the value of Ψ_C , which is 0.314 mrad. However, the former yield decreases with α after the inflection point considerably slower than the latter yield. They fall below 10 % of the yields for the straight bundle at $\alpha = 1.45$ and 0.75 mrad, respectively. This figure also gives the total yield of protons transmitted through the bundle, both through the circular and triangular channels, as a function of α . Its inflection point appears at $\alpha = 0.45$ mrad, and it falls below 10 % of the yield for the straight bundle at $\alpha = 1.25$ mrad.

5.3 Rainbows with long nanotubes

Let us now consider a 1 GeV proton moving through a long (11, 9) single-wall carbon nanotube (Petrović et al., 2008b). The nanotube length, L , is varied from 10 to 500 μm . Such a nanotube is chiral, i.e. its atomic strings spiral around its axis. The z axis of the reference frame coincides with the nanotube axis and its origin lies in the entrance plane of the nanotube. The x and y axes of the reference frame are the vertical and horizontal axes, respectively.

In the calculations we employ the theory of crystal rainbows, which is described in part §3.2 of the chapter. The interaction of the proton and a nanotube atom is described by the Molière's approximation (Molière, 1947) of the Thomas-Fermi interaction potential, which is given by Eq. (13). Since the nanotube is chiral, the interaction potential of the proton and nanotube is obtained by the azimuthal averaging of the Molière's proton-nanotube continuum interaction potential, which is given by Eqs. (14)-(16), with the thermal vibrations of the nanotube atoms taken into account, via Eq. (17); in these equations $I = 1$, $J = 40$, and $\sigma_{th} = 5.3$ pm (Thess et al., 1996). This interaction potential reads

$$U^{th}(x, y) = \frac{16\pi Z_1 Z_2 e^2 R}{3\sqrt{3}a_{CC}^2} \sum_{i=1}^3 \left(\alpha_i + \frac{\sigma_{th}^2 \beta_i^2}{2a^2} \right) K_0(\beta_i R/a) I_0(\beta_i \rho/a), \quad (18)$$

where $a_{CC} = 0.14$ nm is the bond length of the carbon atoms (Saito et al., 2001), $R = 0.69$ nm is the nanotube radius (Saito et al., 2001), $(\alpha_i) = (0.35, 0.55, 0.10)$ and $(\beta_i) = (0.1, 1.2, 6.0)$ are the fitting parameters, $\rho = (x^2 + y^2)^{\frac{1}{2}}$, x and y are the transverse components of the proton position vector, and I_0 denotes the modified Bessel function of the first kind and 0th order Artru et al. (2005). It is evident that $U^{th}(x, y)$ is cylindrically symmetric.

The electronic proton energy loss and dispersion of its transmission angle, caused by its collisions with the nanotube electrons, are not taken into account. The components of the proton impact parameter vector are chosen randomly within the circle around the origin of radius $R - a$. The initial proton velocity vectors are all taken to be parallel to the nanotube axis.

Since $U^{th}(x, y)$ is cylindrically symmetric, the problem we consider is in fact one-dimensional. This means that the rainbow lines in the impact parameter plane and transmission angle plane, if they exist, will show up as the circles. Consequently, it is sufficient to analyze the mapping of the x

axis in the impact parameter plane to the Θ axis in the transmission angle plane, i.e., the $\Theta_x(x)$ deflection function. The abscissas and ordinates of the extrema of this deflection function determine the radii of the rainbow lines in the impact parameter plane and transmission angle plane, respectively.

Figures 11(a)-(d) show the angular distributions of channeled protons along the Θ axis for $L = 10, 50, 100$ and $500 \mu\text{m}$, respectively. The size of a bin along the Θ axis is $0.866 \mu\text{rad}$ and the initial number of protons is 16 656 140. These values enabled us to attain a high resolution of the angular distributions in a reasonable computational time. The angular distributions obtained for $L = 10, 50$ and $100 \mu\text{m}$ contain a central maximum and a number of symmetric pairs of maxima characterized by a sharp decrease of the proton yield on the large angle side; the numbers of symmetric pairs of sharp maxima are one, eight and 15, respectively. The angular distribution obtained for $L = 500 \mu\text{m}$ contains a central maximum and a large number of symmetric pairs of sharp maxima close to each other. The analysis shows that in the region where $|\Theta_x| \leq 0.2 \text{ mrad}$ one can identify 55 pairs of sharp maxima. Figure 11(d) also shows that in the region where $0.041 \text{ mrad} \leq |\Theta_x| \leq 0.058 \text{ mrad}$ there are five pairs of sharp maxima; they are designated by 11-15. In the region in which $|\Theta_x| > 0.2 \text{ mrad}$ the resolution of the angular distribution is not sufficiently high to distinguish easily between the adjacent pairs of sharp maxima.

The $\Theta_x(x)$ deflection functions obtained for $L = 10, 50, 100$ and $500 \mu\text{m}$ are given in Figs. 12(a)-(d), respectively. The deflection functions for $L = 10, 50$ and $100 \mu\text{m}$ contain one, eight and 15 symmetric pairs of extrema, respectively; each pair includes a minimum and a maximum. The analysis shows that the deflection function obtained for $L = 500 \mu\text{m}$ contains 76 symmetric pairs of extrema. Figure 12(d) also gives five pairs of extrema, designated by 11-15, that correspond to the five sharp maxima shown in Fig. 11(d). Each symmetric pair of extrema defines a circular rainbow line in the impact parameter plane and a circular rainbow line in the transmission angle plane. One can observe that each of the deflection functions for $L = 50, 100$ and $500 \mu\text{m}$ has two envelopes, one of them connecting its extrema designated by odd numbers and the other connecting its extrema designated by even numbers, and that it oscillates between these envelopes.

The comparison of Figs. 11(a)-(c) and Figs. 12(a)-(c) shows that the abscissas of the pairs of sharp maxima of each angular distribution of channeled protons along the Θ_x axis coincide with the ordinates of the corresponding pairs of extrema of the accompanying $\Theta_x(x)$ deflection function. One can

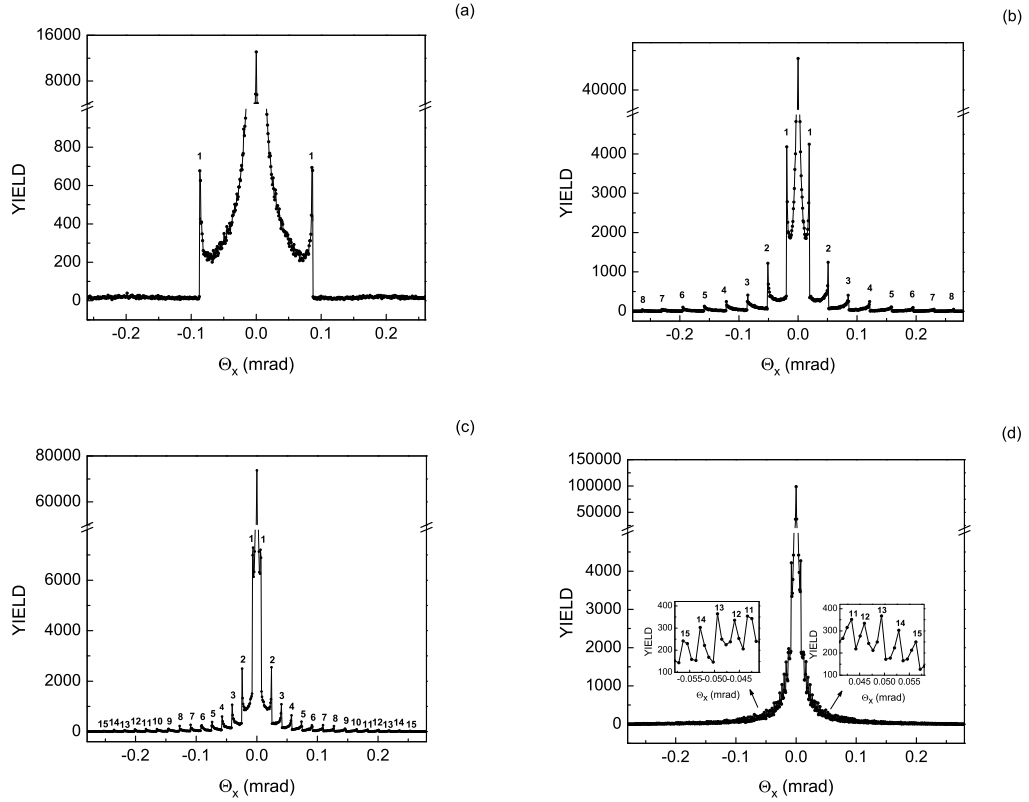


Figure 11: The angular distributions along the Θ_x axis of 1 GeV protons channeled through the (11, 9) SWCNTs of the length of (a) 10 μm , (b) 50 μm , (c) 100 μm and (d) 500 μm .

draw the same conclusion for the pairs of sharp maxima of the angular distribution given in Fig. 11(d) and the corresponding pairs of extrema of the deflection function given in Fig. 12(d), in spite of the fact that in the region where $|\Theta_x| > 0.2$ mrad it is not possible to identify the additional 21 pairs of sharp maxima of the angular distribution. Hence, it is clear that the sharp maxima of the angular distributions can be attributed to the rainbow effect. The bright and dark sides of the rainbows are the small and large angle sides of the corresponding sharp maxima.

Figures 12(a)-(d) show clearly that the number of rainbows generated by the transmitted protons increases and the average distance between them decreases as L increases. These two dependences, for L between 50 and 500 μm , are given in Fig. 13. The numbers and positions of the rain-

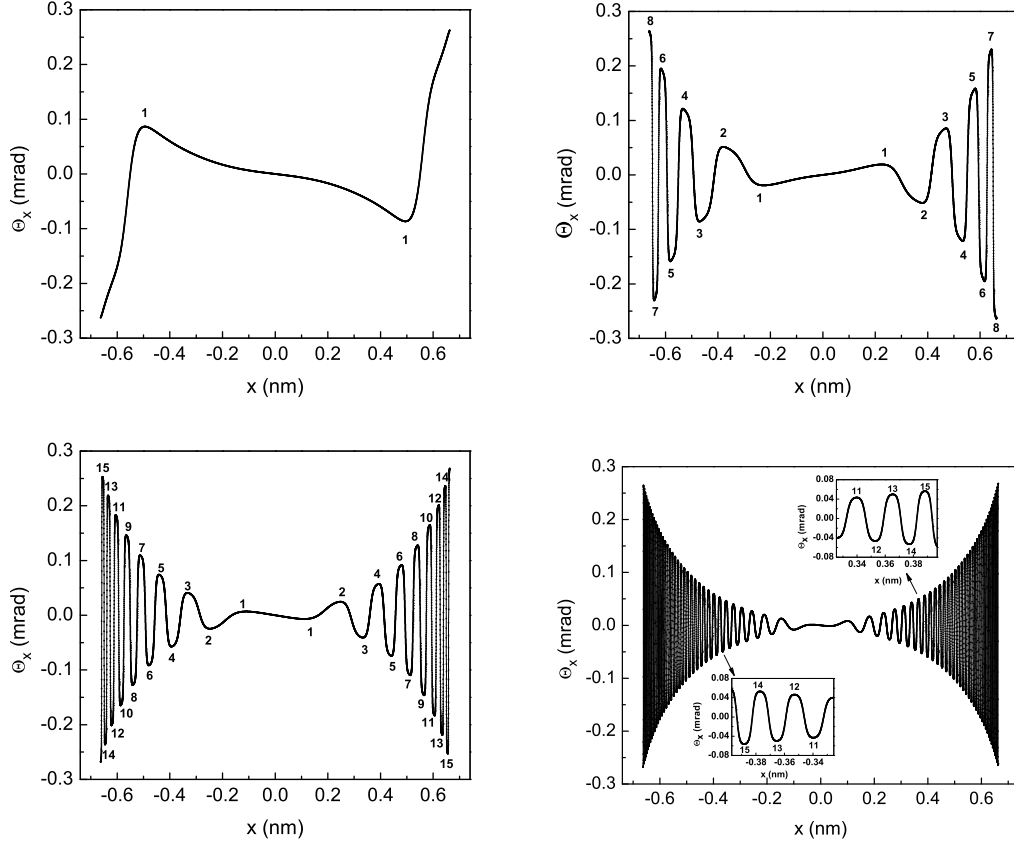


Figure 12: The deflection functions Θ_x of the x axis in the impact parameter plane for 1 GeV protons channeled through the (11, 9) SWCNTs of the length of (a) 10 μm , (b) 50 μm , (c) 100 μm and (d) 500 μm .

bows are determined from the accompanying $\Theta_x(x)$ deflection functions. The analysis shows that the former dependence can be approximated excellently by fitting function , where $a_1 = 0.15$ is the fitting parameter. The latter dependence can be approximated excellently by fitting function $f_2 = a_2 \exp(-L/b_2) + a_3 \exp(-L/b_3)$, where $a_2 = 0.072$ mrad, $b_2 = 42.6$ μm , $a_3 = 0.015$ mrad and $b_3 = 340.5$ μm are the fitting parameters. These fitting functions are also shown in Fig. 13. When the nanotube becomes sufficiently long for the average distance between the rainbows to become smaller than the resolution of the angular distribution, one cannot distinguish between the adjacent rainbows. This means that the rainbows disappear and the an-

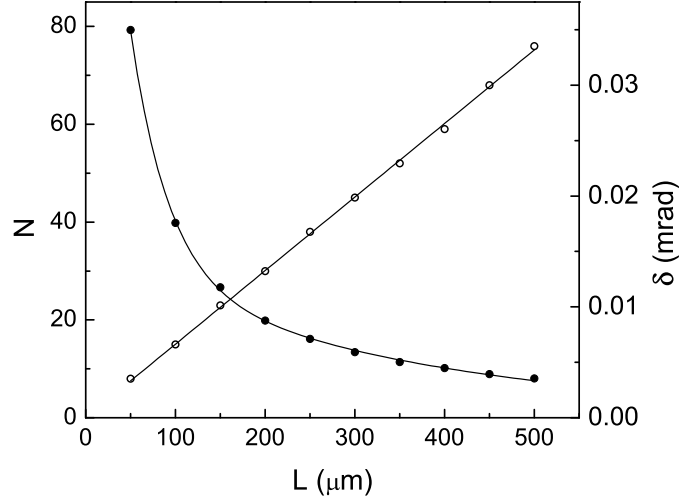


Figure 13: The dependences of the number of circular rainbows in the angular distributions of 1 GeV protons channeled through the (11, 9) single-wall carbon nanotubes – N , open circles, and the average distance between them – δ , closed circles, on the nanotube length – L . The full lines represent the fitting curves.

gular distribution becomes a bell-shaped one. The analysis shows that, in parallel, the spatial distribution of channeled protons in the exit plane of the nanotube also becomes a bell-shaped one. Hence, one can say that, when the nanotube becomes sufficiently long, the angular and spatial distributions equilibrate, and, as one would expect, this does not happen in accordance with the ergodic hypothesis Barrett (1973). We call this route to equilibration, which is characterized by the linear increase of the number of rainbows and the exponential decrease of the distance between them as L increases, the rainbow route to equilibration.

Recently, a theoretical analysis of the channeling of 1 GeV protons through the long (10, 10) single-wall carbon nanotubes has been reported Petrović et al. (2009). The angular distributions of transmitted protons were generated for L between 10 and 100 μm . The obtained results show that when $L < 30 \mu\text{m}$ the transverse lattice structure of the nanotube can be deduced from the angular distribution. When $L \geq 40 \mu\text{m}$ the angular distribution contains the concentric circular ridges whose number increases linearly and the distance between them decreases exponentially as L increases, in a similar way as in

the above described case of (11, 9) nanotubes. Consequently, these ridges can be attributed to the rainbow effect.

The above presented results demonstrate that one can employ the angular distributions of protons channeled through long carbon nanotubes for their characterization. Namely, it seems that each type of nanotube for each value of L has a characteristic pattern of concentric circular ridges, and that this can be checked experimentally. However, an easier way to check this experimentally would be to vary the proton kinetic energy rather than L . This method of characterization of nanotubes would be complementary to the method proposed in part §5.1 of this chapter.

6 Dynamic polarization effect in proton channeling through short nanotubes

In this part of the chapter we shall investigate how the angular and spatial distributions of protons channeled through a short (11, 9) single-wall carbon nanotube in vacuum or embedded in a dielectric medium is influenced by the effect of dynamic polarization of the nanotube atoms valence electrons (Borka et al., 2006a, 2008b,a). The magnitude of the proton velocity vector, v , is varied between 3 and 8 a.u., corresponding to the proton kinetic energy between 0.223 and 1.59 MeV, respectively. It is expected that the dynamic polarization effect, which is induced by the proton, is pronounced in this range of its kinetic energy. The nanotube length, L , is varied between 0.1 and 0.8 μm . We shall also explore the influence of the angle of the initial proton velocity vector relative to the nanotube axis on the angular distribution of protons channeled through a short (11, 9) nanotube in vacuum for $v = 3$ a.u. and $L = 0.2 \mu\text{m}$ (Borka et al., 2010).

The z axis of the reference frame coincides with the nanotube axis and its origin lies in the entrance plane of the nanotube. The x and y axes of the reference frame are the vertical and horizontal axes, respectively. The calculations are performed using the theory of crystal rainbows, which is described in part §3.2 of the chapter. The thermal vibrations of the nanotube atoms are not taken into account. The electronic proton energy loss and dispersion of its transmission angle, caused by its collisions with the nanotube electrons, are neglected too. The components of the proton impact parameter vector are chosen randomly within the circle around the origin of radius $R - a$,

where R is the nanotube radius, $a = [9\pi^2/(128Z_2)]^{\frac{1}{3}} a_0$ the screening radius of the nanotube atom, and a_0 the Bohr radius. The initial proton velocity vectors are all taken to be parallel to the nanotube axis.

6.1 Rainbows with short nanotubes in vacuum

The system under consideration here is a proton moving through a short (11, 9) single-wall carbon nanotube in vacuum for $v = 3$ a.u. and $L = 0.1\text{-}0.3 \mu\text{m}$ (Borka et al., 2006a); the corresponding proton kinetic energy is 0.223 MeV. This nanotube is chiral.

The interaction of the proton and a nanotube atom is described by the Doyle-Turner interaction potential (Doyle & Turner, 1968). Since the nanotube is chiral, the static part of the interaction potential of the proton and nanotube is obtained by the azimuthal averaging of the Doyle-Turner proton-nanotube continuum interaction potential (Lindhard, 1965; Zhevago & Glebov, 1998, 2000); the number of atomic strings of the nanotube is $J = 40$. This interaction potential, in atomic units, is

$$U_s(x, y) = \frac{32\pi Z_1 Z_2 R}{3\sqrt{3}a_{CC}^2} \sum_{i=1}^4 \alpha_i \delta_i^2 I_0(\delta_i^2 R \rho) \exp[-\delta_i^2(\rho^2 + R^2)], \quad (19)$$

where $(\gamma_i) = (0.115, 0.188, 0.072, 0.020)$ and $(\delta_i) = (0.547, 0.989, 1.982, 5.656)$ are the fitting parameters (in a.u.), $\rho = (x^2 + y^2)^{\frac{1}{2}}$, x and y are the transverse components of the proton position vector, and I_0 denotes the modified Bessel function of the first kind and 0th order. It is clear that $U_s(x, y)$ is repulsive and cylindrically symmetric.

The dynamic polarization effect is treated by a two-dimensional hydrodynamic model of the nanotube atoms valence electrons based on a jellium-like description of the ion cores on the nanotube walls (Mowbray et al., 2004a,b; Borka et al., 2006a). This model includes the axial and azimuthal averaging as in the case of $U_s(x, y)$. As a result, the dynamic part of the interaction potential of the proton and nanotube is

$$U_d(x, y) = \frac{Z_1^2}{\pi} \sum_{l=-\infty}^{\infty} P \int_0^{\infty} K_l^2(kR) \frac{4\pi n_0 R (k^2 + l^2/R^2)}{(kv)^2 - \omega_l^2(k)} I_l^2(k\rho) dk, \quad (20)$$

where

$$\omega_l^2(k) = (k^2 + l^2/R^2) [4\pi n_0 R I_l(kR) K_l(kR) + v_s^2] \quad (21)$$

is the square of the angular frequency of the proton induced oscillations of the nanotube electron gas of angular mode l and longitudinal wave number k , $n_0 = 0.428$ the ground state density of the nanotube electron gas, $v_s = (\pi n_0)^{\frac{1}{2}}$ is the velocity of propagation of the density perturbations of the nanotube electron gas, $0 \leq \rho < R$, I_l and K_l denote the modified Bessel function of the first and second kinds and l^{th} order, respectively, and P designates that only the principal part of the integral is taken into account. One can see that $U_d(x, y)$, which is also called the image interaction potential of the proton and nanotube, is attractive and cylindrically symmetric. Thus, the total interaction potential of the proton and nanotube is

$$U(x, y) = U_s(x, y) + U_d(x, y). \quad (22)$$

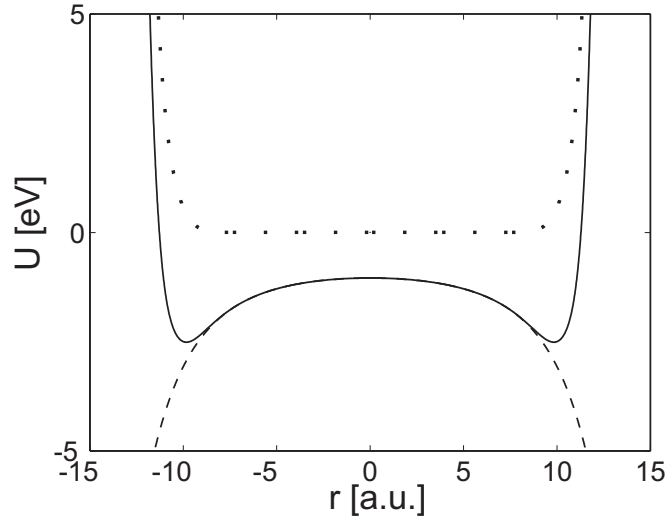


Figure 14: The total interaction potential of the proton and nanotube, $U(x, y)$, along the x axis in the interval $(-R, R)$ for $v = 3$ a.u - solid line. The static and dynamic parts of the interaction potential are also shown - dotted and dashed lines, respectively.

Figure 14 shows the total interaction potential of the proton and nanotube, $U(x, y)$, along the x axis in interval $(-R, R)$ for $v = 3$ a.u. (Borka et al.,

2006a; Petrović et al., 2008a). The static and dynamic parts of the interaction potential are also shown in the figure. One can see that due to the inclusion of the image interaction potential the total interaction potential of the proton and nanotube has two inflection points. They appear for $x = \pm 8.1$ a.u. If the nanotube we consider is short, the corresponding $\Theta_x(x)$ deflection function will have a pair of symmetric extrema appearing for the values of x close to ± 8.1 a.u.

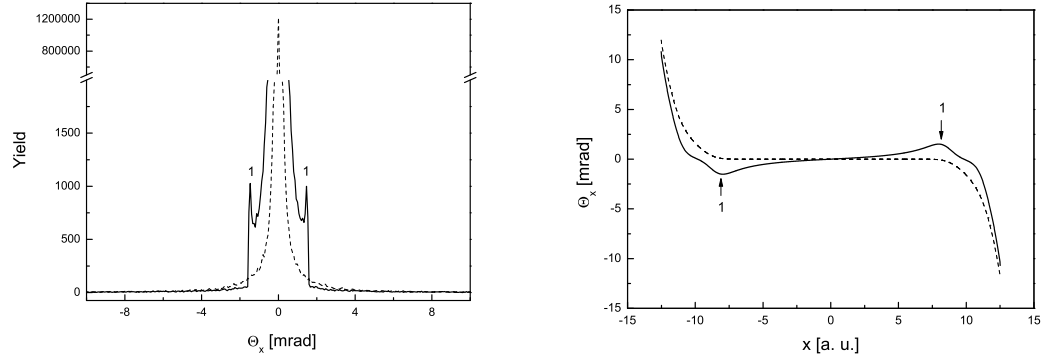


Figure 15: (a) The angular distributions along the Θ_x axis of protons transmitted through a (11, 9) single-wall carbon nanotubes for $v = 3$ a.u. and $L = 0.1 \mu\text{m}$ with and without the dynamic polarization effect included – solid and dashed lines, respectively. (b) The corresponding $\Theta_x(x)$ deflections functions.

The angular distribution of transmitted protons along the Θ_x axis for $v = 3$ a.u. and $L = 0.1 \mu\text{m}$ is given in Fig. 15(a) (Borka et al., 2006a). This figure also shows the corresponding angular distribution when the image interaction potential of the proton and nanotube is not included. The size of a bin along the Θ_x axis is equal to 0.066 mrad and the initial number of protons is 3 141 929. One can see that a central maximum and a pair of symmetric peripheral maxima appear in the angular distribution when the image interaction potential is included; the peripheral maxima are labeled by 1. Figure 15(b) shows the $\Theta_x(x)$ deflection functions corresponding to the angular distributions given in Fig. 15(a). It is evident that the deflection function without the image interaction potential taken into account has no extrema. On the other hand, the deflection function with the image interaction potential taken into account exhibits a pair of symmetric extrema; they are also labeled by 1. The analysis shows that the two peripheral maxima

of the angular distribution are connected to the two extrema of the deflection function. Therefore, we conclude that they are the rainbow maxima, and that they occur as a consequence of the inclusion of the dynamic polarization effect. Besides, one should note that the extrema of the deflection function appear for $x = \pm 8.0$ a.u. Since these positions are close to the positions of the inflection points of the total interaction potential, one should conclude that the nanotube in question is short.

We have established that for $v = 3$ a.u. and $L = 0.2 \mu\text{m}$ the angular distribution of transmitted protons along the Θ_x axis contains three pairs of rainbow maxima, and that for $v = 3$ a.u. and $L = 0.3 \mu\text{m}$ the angular distribution includes five pairs of rainbow maxima (Borka et al., 2006a). All these maxima are attributed to the image interaction potential of the proton and nanotube.

6.2 Rainbows with short nanotube embedded in dielectric media

Experimentally, the main problem that prevent the observation of ion channeling through carbon nanotubes is the problem of ordering, straightening and holding nanotubes. The most promising method enabling us to solve this problem is based on the growing of nanotubes inside the holes in a dielectric medium (Zhu et al., 2005; Berdinsky et al., 2008). Besides, in many applications of nanotubes it is desirable to have them embedded in SiO_2 (Tsetseris & Pantelides, 2006), or clamped by a Ni shield (Guerret-Piécourt et al., 1994; Mišković, 2007).

When a nanotube is embedded in a dielectric medium, the static part of its interaction potential with the proton is the same as in the case when it is in vacuum, which is given by Eq. (19). The dynamic part of the interaction potential is obtained by a hydrodynamic model of the nanotube atoms valence electrons based on the jellium-like description of the ion cores on the nanotube walls, as in the case when the nanotube is in vacuum, but extended to include the polarization of the dielectric boundary (Mowbray et al., 2007; Borka et al., 2008b). It should be noted that this model has also been applied successfully in the related area of ion interaction with dielectric supported sheets of carbon atoms (Radović et al., 2007, 2009).

Figure 16(a) shows the angular distribution along the Θ_x axis of protons transmitted through a (11, 9) single-wall carbon nanotube embedded in SiO_2

for $v = 5$ a.u. and $L = 0.5 \mu\text{m}$ (Borka et al., 2008b); the corresponding proton kinetic energy is 0.619 MeV. This figure also shows the corresponding angular distribution when the nanotube is in vacuum. The size of a bin along the Θ_x axis is equal to 0.0213 mrad and the initial number of protons is 3 141 929. One can see a central maximum and only one pair of symmetric peripheral maxima, labeled by 1_d , when the nanotube is embedded in SiO_2 , in comparison with a central maximum and three pairs of symmetric peripheral maxima, labeled by 1, 2' and 2'', when the nanotube is in vacuum. Figure 16(b) gives the $\Theta_x(x)$ deflection functions corresponding to the angular distributions given in Fig. 16(a). We have found that each peripheral maximum of each angular distribution is connected to an extremum of the corresponding deflection function. Hence, all the peripheral maxima are the rainbow maxima.

Let us now analyze the spatial distributions along the x axis in the exit plane of the nanotube of protons transmitted through a (11, 9) single-wall carbon nanotube embedded in SiO_2 and in vacuum for $v = 5$ a.u. and $L = 0.5 \mu\text{m}$ (Borka et al., 2008a). It is given in Fig. 16(c). The size of a bin along the Θ_x axis is equal to 0.3 a.u. and the initial number of protons is 3 141 929. In the former case the spatial distribution contains a central maximum and three pairs of symmetric peripheral maxima, labeled by 1_d , 2_d and 3_d , and in the latter case the spatial distribution includes a central maximum and four pairs of symmetric peripheral maxima, labeled by 1_i , 2_i , 3_i and 4_i . The maxima designated by 2_d , 3_d , 3_i and 4_i are very weak. Figure 16(d) gives the mappings of the x_0 axis in the entrance plane of the nanotube to the x axis in its exit plane corresponding to the spatial distributions given in Fig. 16(c). It is evident that when the nanotube is embedded in SiO_2 , the mapping has six symmetric extrema, labeled by 1_d , 2_d and 3_d . When the nanotube is in vacuum, the mapping has eight symmetric extrema, labeled by 1_i , 2_i , 3_i and 4_i . Extrema 2_d , 3_d , 3_i and 4_i are very sharp and lie near the nanotube wall. In each case the ordinate of the extremum of the mapping coincides with the abscissa of the corresponding peripheral maximum of the spatial distribution. Therefore, these maxima are attributed to the rainbow effect.

Figure 17(a) gives the angular distribution along the Θ_x axis of protons channeled through a (11, 9) single-wall carbon nanotube embedded in SiO_2 , Al_2O_3 and Ni and in vacuum for $v = 8$ a.u. and $L = 0.8 \mu\text{m}$ (Borka et al., 2008b); the corresponding proton kinetic energy is 1.59 MeV. The size of a bin along the Θ_x axis is equal to 0.0213 mrad and the initial number of

protons is 3 141 929. The angular distributions obtained with the embedded nanotube contain one central maximum and two symmetric peripheral maxima, labeled by 1_d . It is clear that these positions do not depend much on the type of medium surrounding the nanotube. This can be explained by the fact that in these cases the dependences of the image force acting on the proton on x are close to each other (Borka et al., 2008b). When the nanotube is in vacuum, the angular distribution contains a central maximum and no symmetric peripheral maxima. Figure 17(b) shows the $\Theta_x(x)$ deflection functions corresponding to the angular distributions shown in Fig. 17(a). It is clear that in the cases of embedded nanotubes the deflection functions contain two pairs of symmetric extrema. The analysis shows that the two peripheral maxima appearing in the angular distributions obtained with the embedded nanotube are connected to the former pair of extrema of the corresponding deflection functions, also labeled by 1_d . This means that these maxima are due to the rainbow effect. The angular distributions obtained with the embedded nanotube do not include any maxima that would be connected to the latter pair of extrema of the corresponding deflection functions, lying close to the nanotube wall. It is also clear that in the case of nanotube in vacuum the deflection function includes only one pair of symmetric extrema, lying close to the nanotube wall. However, as it has been already said, the angular distribution obtained with the nanotube in vacuum does not have any maxima that would be connected to the pair of extrema of the corresponding deflection function.

Now, we are going to consider the spatial distributions along the x axis in the exit plane of the nanotube of protons channeled through a (11, 9) single-wall carbon nanotube embedded in SiO_2 , Al_2O_3 and Ni and in vacuum for $v = 8$ a.u. and $L = 0.8 \mu\text{m}$ (Borka et al., 2008a). They are shown in Fig. 17(c). The size of a bin along the Θ_x axis is equal to 0.3 a.u. and the initial number of protons is 3 141 929. All these spatial distributions contain a central maximum and three pairs of symmetric peripheral maxima. In the cases of embedded nanotubes the peripheral maxima are labeled by 1_d , 2_d and 3_d , and in the case of nanotube in vacuum the peripheral maxima are labeled by 1_i , 2_i and 3_i . One can see that the angular distributions obtained with the embedded nanotubes do not differ much from each other, and that they differ from the angular distribution obtained with the nanotube in vacuum. The spatial distributions obtained with the nanotube embedded in SiO_2 and Ni almost coincide. Figure 17(d) shows the mappings of the x_0 axis in the entrance plane of the nanotube to the x axis in its exit plane corresponding

to the spatial distributions shown in Figure 17(c). One can observe that all these mappings include three pairs of symmetric extrema. In the cases of embedded nanotubes the extrema of the mappings are labeled by 1_d , 2_d and 3_d , and in the case of nanotube in vacuum the extrema are labeled by 1_i , 2_i and 3_i . In each case the ordinate of the extremum of the mapping coincides with the abscissa of the corresponding peripheral maximum of the spatial distribution. Therefore, these maxima are the rainbow maxima.

Let us now compare the above described angular and spatial distributions of channeled protons, obtained for $v = 5$ a.u. and $L = 0.5 \mu\text{m}$, and for $v = 8$ a.u. and $L = 0.8 \mu\text{m}$. All of them are characterized by the same proton dwell time, i.e., the same duration of the process of proton channeling. When the nanotube is in vacuum, the numbers of rainbow maxima of the angular and spatial distributions are larger in the former case than in the latter case. This is attributed to the weakening of the image force acting on the proton with the increase of v . On the other hand, when the nanotube is embedded, the numbers of rainbow maxima of the angular and spatial distributions is the same in the former and latter cases. This persistency of the rainbow effect with the increase of v is explained by the increase of the image force due to the polarization of the dielectric boundary.

Our findings indicate that a dielectric medium surrounding carbon nanotubes can influence their properties. Also, the changing of the spatial distribution of channeled protons with their kinetic energy we have demonstrated, based on the changing of the dynamic polarization effect, may be used to probe the atoms or molecules intercalated in the nanotubes. Besides, we think that nanotubes could be employed to produce nanosized ion beams for applications in biomedicine.

6.3 Donut effect with protons and a short nanotube in vacuum

In ion channeling experiments the always present questions are the questions of ion beam misalignment and divergence. Therefore, it is important to explore how the dynamic polarization effect influences the angular and spatial distributions of ions channeled through carbon nanotubes when the initial ion velocity vector is not parallel to the nanotube axis. We are going to focus on the angular distribution of protons channeled through a (11, 9) single-wall carbon nanotube in vacuum for $v = 3$ a.u. and $L = 0.2 \mu\text{m}$ and for the

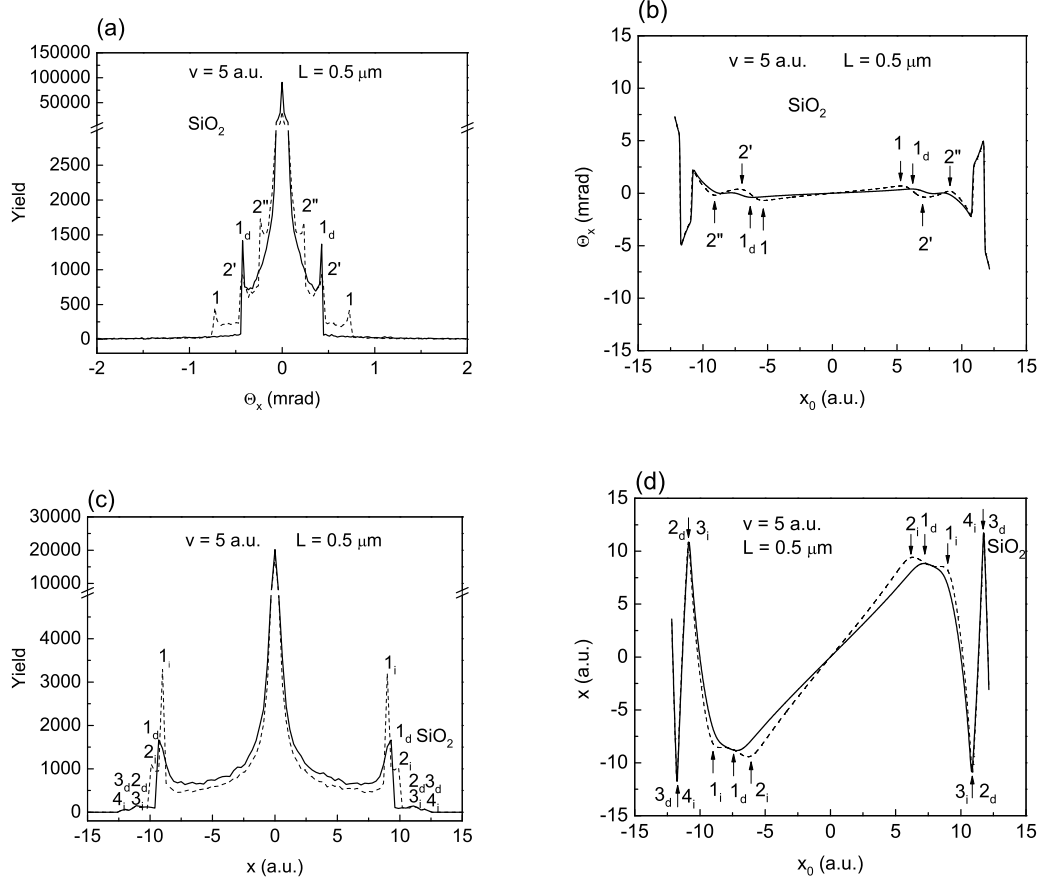


Figure 16: (a) The angular distributions along the Θ_x axis of protons transmitted through a (11, 9) single-wall carbon nanotube embedded in SiO₂ and in vacuum for $v = 5$ a.u. and $L = 0.5 \mu\text{m}$ - solid and dashed lines, respectively. (b) The corresponding deflections functions. (c) The corresponding spatial distributions along the x axis in the exit plane of the nanotube - solid and dashed lines, respectively. (d) The corresponding mappings of the x_0 axis in the entrance plane of the nanotube to the x axis in its exit plane - solid and dashed lines, respectively.

angle of the initial proton velocity vector relative to the nanotube axis, φ , between 0 and 10 mrad (Borka et al., 2010); the corresponding proton kinetic energy is 0.223 MeV. In this case the critical angle for channeling is $\Psi_C = 11$ mrad. It should be noted that the inclusion of a dielectric medium around

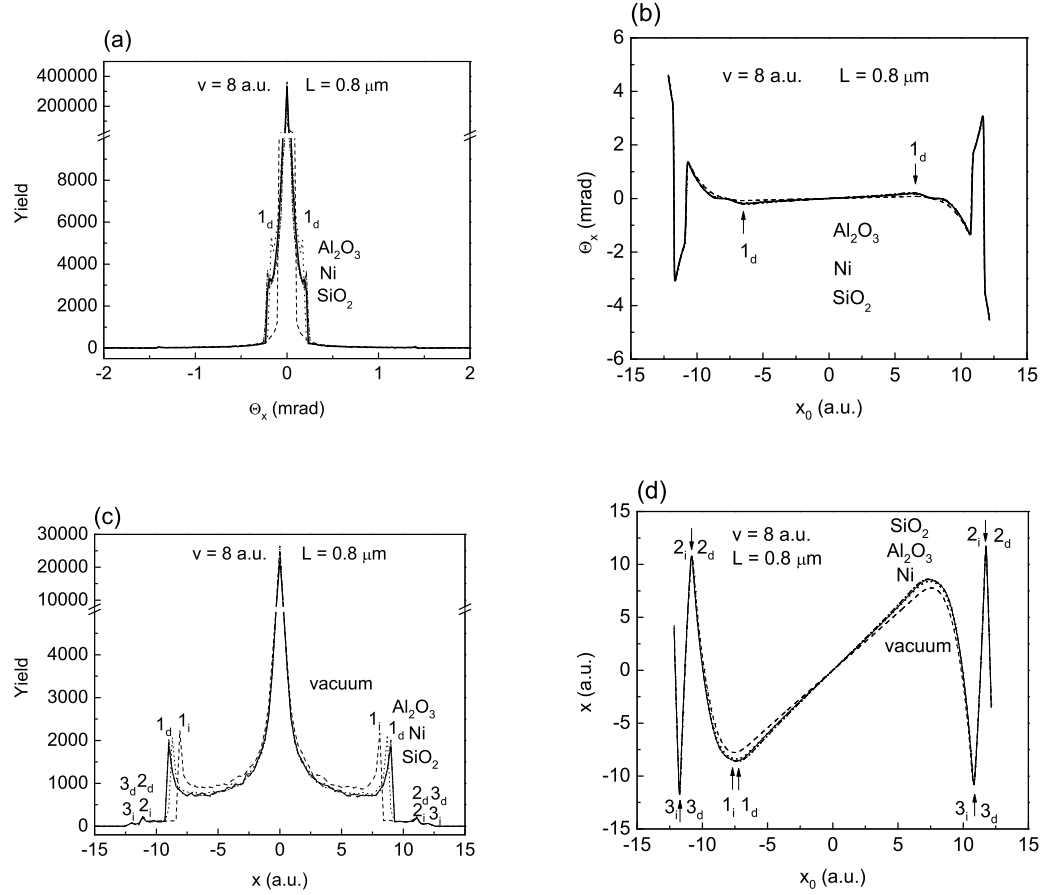


Figure 17: (a) The angular distributions along the Θ_x axis of protons transmitted through a (11, 9) single-wall carbon nanotube embedded in SiO_2 , Al_2O_3 and Ni and in vacuum for $v = 8$ a.u. and $L = 0.8 \mu\text{m}$ - solid, dotted and dash dotted lines and dashed line, respectively. (b) The corresponding $\Theta_x(x)$ deflections functions. (c) The corresponding spatial distributions along the x axis in the exit plane of the nanotube - solid and dashed lines, respectively. (b) The corresponding mappings of the x_0 axis in the entrance plane of the nanotube to the x axis in its exit plane - solid and dashed lines, respectively.

the nanotube will modify the results of the calculation only slightly.

It is well-known that when φ is close to Ψ_C , the angular distribution of ions transmitted through crystal channels takes the shape of a donat

(Chadderton, 1970; Rosner et al., 1978; Andersen et al., 1980). This effect is called the donut effect. It has been explained afterwards by the theory of crystal rainbows (Nešković et al., 2002; Borka et al., 2003). It must be noted that the donut effect has been observed in computer simulations of ion propagation through nanotubes (Zhevago & Glebov, 1998, 2000). However, the authors did not connect the obtained results to the rainbow effect.

Figure 18(a) shows the angular distribution of transmitted protons for $\varphi = 10$ mrad, being close to Ψ_C (Borka et al., 2010). The image force acting on the proton is taken into account. One can see clearly that it has a ring-like structure, and that the yield of protons along the ring is very high. This is the fully developed donut effect. The corresponding rainbow lines in the transmission angle plane are shown in Fig. 18(b). These lines demonstrate that the structure of the angular distribution, including the donut effect, is due to the rainbow effect. We have established that the influence of the dynamic polarization effects on the angular distribution is significant for φ between 0 and $\Psi_C/2$. However, when φ becomes close to Ψ_C , this influence is reduced strongly (Borka et al., 2010). This means that the contribution of the dynamic polarization effect to the donut effect is minor.

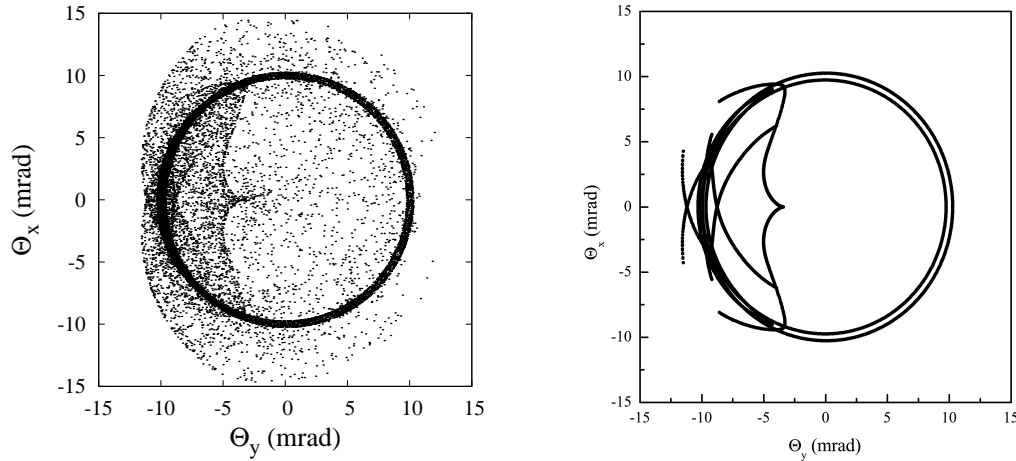


Figure 18: (a) The angular distribution of protons transmitted through a (11, 9) single-wall carbon nanotube for $v = 3$ a.u., $L = 0.2 \mu\text{m}$ and $\varphi = 10$ mrad. The image force acting on the proton is taken into account. (b) The corresponding rainbow pattern in the transmission angle plane.

7 Dynamic polarization effect in proton channeling through short nanotubes

The channeling star effect was observed for the first time in the early experiments on ion transmission through axial crystal channels (Gemmell, 1974). The characteristic "arms" of a channeling star were attributed to the ions moving along the planar channels that cross the axial channel. It must be noted that such a motion can occur only when the ion beam divergence is larger than the critical angle for channeling (Petrović et al., 2002). Usually, the effect has been used for precise alignment of the ion beam with the channel axis.

We are going to describe here the channeling star effect in the transmission of protons through the bundles of (10, 10) single-wall carbon nanotubes (Borka et al., 2006b). The initial proton energy is 1 GeV and the bundle length is varied between 2.2 to 14.3 μm , corresponding to the reduced bundle length associated with the protons moving close to the centers of the triangular channels of the bundle, Λ_2 , between 0.15 and 1, respectively (see part §4 of this review). The study is focused on the problem of mutual orientation of the neighboring nanotubes within the bundle, which has not been resolved yet (Kwon & Tománek, 2000). The nanotubes in question are achiral. It is assumed that they form a bundle whose transverse cross-section can be described via a hexagonal or rhombic superlattice with one nanotube per primitive cell (Thess et al., 1996). We choose the y axis of the reference frame to coincide with the bundle axis and its origin to lie in the entrance plane of the bundle. The arrangement of the nanotubes is such that their axes intersect the x and y axes of the reference frame, which are the vertical and horizontal axes, respectively (Petrović et al., 2005c). We take into account the contributions of the nanotubes lying on the two nearest rhombic coordination lines, relative to the center of the (rhombic) primitive cell of the superlattice. The initial proton beam axis coincides with the bundle axis. The proton beam divergence angle is chosen to be $\Omega_d = 6\psi_c$, where $\psi_c = 0.314$ mrad is the critical angle for channeling. The calculations are performed using the theory of crystal rainbows, which is described in part §3.2 of this review. The interaction of the proton and a nanotube atom is described by the Molière's approximation (Molière, 1947) of the Thomas-Fermi interaction potential, which is given by Eq. (13). The application of the continuum approximation gives the Molière's proton-bundle continuum

interaction potential, which is defined by Eq. (14). The number of nanotubes within the bundle $I = 16$, the number of atomic strings of a nanotube $J = 40$, and the distance between the atoms of an atomic string $d = 0.24$ nm. The thermal vibrations of the nanotube atoms are taken into account. This is done by Eq. (17). The one-dimensional thermal vibration amplitude of the nanotube atoms $\sigma_{th} = 5.3$ pm (Hone et al., 2000).

The electronic proton energy loss and dispersion of its proton transmission angle, caused by its collisions with the nanotube electrons, are taken into account. For the specific proton energy loss we use expression

$$-\frac{dE_e}{dz} = \frac{4\pi Z_1^2 e^4}{m_e v^2(z)} n_e \left[\ln \frac{2m_e \gamma^2 v^2(z)}{\hbar \omega_e} - \beta^2 \right], \quad (23)$$

where m_e is the electron mass, $v(z)$ the magnitude of the proton velocity vector, $\beta = v(z)/c$, c the speed of light, $\gamma^2 = (1 - \beta^2)^{-1}$, $n_e = (\partial_{xx} + \partial_{yy})U^{th}(x, y)/4\pi$ the average along the z axis of the density of the nanotube electron gas, $U^{th}(x, y)$ the Molière's proton-bundle continuum interaction potential with the effect of thermal vibrations of the nanotube atoms taken into account, \hbar the reduced Planck constant, and $\omega_e = (4\pi e^2 n_e / m_e)^{\frac{1}{2}}$ the angular frequency of the proton induced oscillations of the nanotube electron gas. For the specific change of the dispersion of the proton transmission angle we use expression

$$\frac{d\Omega_e^2}{dz} = \frac{m_e}{m_p^2 v^2(z)} \left(-\frac{dE_e}{dz} \right), \quad (24)$$

where m_p is the (relativistic) proton mass. The corresponding standard deviations of the components of the proton transmission angle, Θ_x and Θ_y , are $\Omega_{ex} = \Omega_{ey} = \Omega_e / \sqrt{2}$.

The nanotube diameter is 1.34 nm (Saito et al., 2001), and the distance between the axes of two neighboring nanotubes is 1.70 nm (Thess et al., 1996). The diameter of the bundle is chosen to be 169.64 nm, corresponding to 100 nanotubes lying on the y axis. The components of the proton impact parameter vector are chosen uniformly within the region of the bundle. For each proton impact parameter the x and y components of its initial velocity, v_{0x} and v_{0y} , respectively, are chosen within the Gaussian distributions with the standard deviations $\Omega_{bx} = \Omega_{by} = \Omega_b / \sqrt{2}$, where Ω_b is the proton beam divergence angle. The initial number of protons is 859 144.

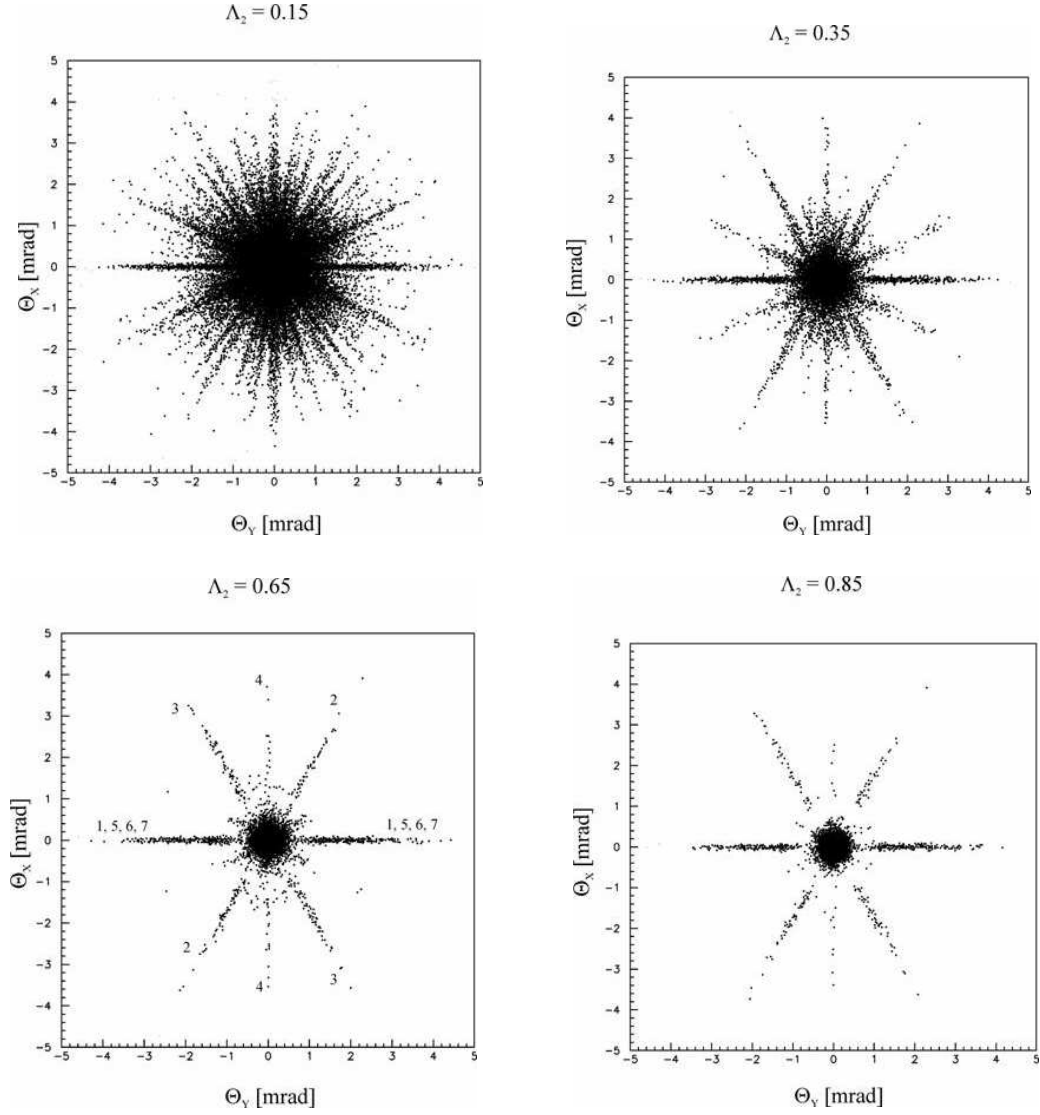


Figure 19: The angular distributions of 1 GeV protons transmitted through the bundles of (10, 10) single-wall carbon nanotubes of the reduced lengths (a) $\Lambda_2 = 0.15$, (b) $\Lambda_2 = 0.35$, (c) $\Lambda_2 = 0.65$, and (d) $\Lambda_2 = 0.85$. The proton beam divergence angle is $\Omega_d = 1.884$ mrad.

Figure 19 show the angular distributions of transmitted protons for $\Lambda_2 = 0.15, 0.35, 0.65$ and 0.85 . For $\Lambda_2 = 0.15$ a channeling star is clearly visible in the angular distribution, and one can distinguish its 40 arms. One can

connect this to the fact that each nanotube has 40 atomic strings. This means that the channeling star effect can be used to learn about the transverse structure of a nanotube. For $\Lambda_2 = 0.35$, 12 arms of the channeling star are still visible, while for $\Lambda_2 = 0.65$ and 0.85 , eight arms remain, with the intensity being lower in the latter case. The analysis shows that the observed intensity lowering and disappearance of the arms as Λ_2 increases can be attributed to the process of proton dechanneling, which is very pronounced since $\Omega_d \gg \psi_c$. For $\Lambda_2 > 1$ the channeling star does not exist any more.

Let us now concentrate on the channeling star for $\Lambda_2 = 0.65$. It has two arms lying along the Θ_x axis, two arms lying along the Θ_y axis, two arms lying along the line defined by $\varphi = \tan^{-1}(\Theta_y/\Theta_x) = n\pi/3$ and $7\pi/6$, and two arms lying along the line defined by $\varphi = 5\pi/6$ and $11\pi/6$. Figure 20 show the components of the proton impact parameter vectors, within the (rhombic) primitive cell of the superlattice, that correspond to the arms of this channeling star. They are selected taking that the proton transmission angle $\Theta = (\Theta_x^2 + \Theta_y^2)^{\frac{1}{2}} \geq 1.6$ mrad. The analysis shows that these impact parameter vectors are located between seven classes of pairs of parallel lines, representing seven classes of pairs of planes defined by the atomic strings of the nanotubes, which are parallel to the bundle axis. There are two equivalent pairs of planes designated by 1, one pair designated by 2, and one pair designated by 3, which are shown in Fig. 20(a), and two equivalent pairs of planes designated by 4, four equivalent pairs designated by 5, four equivalent pairs designated by 6, and four equivalent pairs designated by 7, which are shown in Fig. 20(b). Each pair of planes defines a planar channel, which corresponds to two opposite arms of the channeling star. The pairs of planes that are parallel to each other correspond to the same two opposite arms. In accordance with this, the arms shown in Fig. 19(c) are designated by 4, by 1, 5, 6 and 7, by 2, and by 3.

In order to analyze the sensitivity of the channeling star effect to the mutual orientation of the neighboring nanotubes within the bundle, we rotated each nanotube about its axis by $\pi/60$ counterclockwise relative to its assumed position 4.2. The resulting angular distribution of transmitted protons, for $\Lambda_2 = 0.65$, is given in Fig. 21. In this case the channeling star also has eight arms, as the one given in Fig. 19(c), but the arrangement of its arms is different. Two of the arms lie along the Θ_y axis, two arms lie along the line defined by $\varphi = \pi/6$ and $7\pi/6$, two arms lie along the line defined by $\varphi = 2\pi/6$ and $= 8\pi/6$, and two arms lie along the line defined by $\varphi = 5\pi/6$ and $11\pi/6$. Figure 22 show the components of the proton impact parameter vectors, within

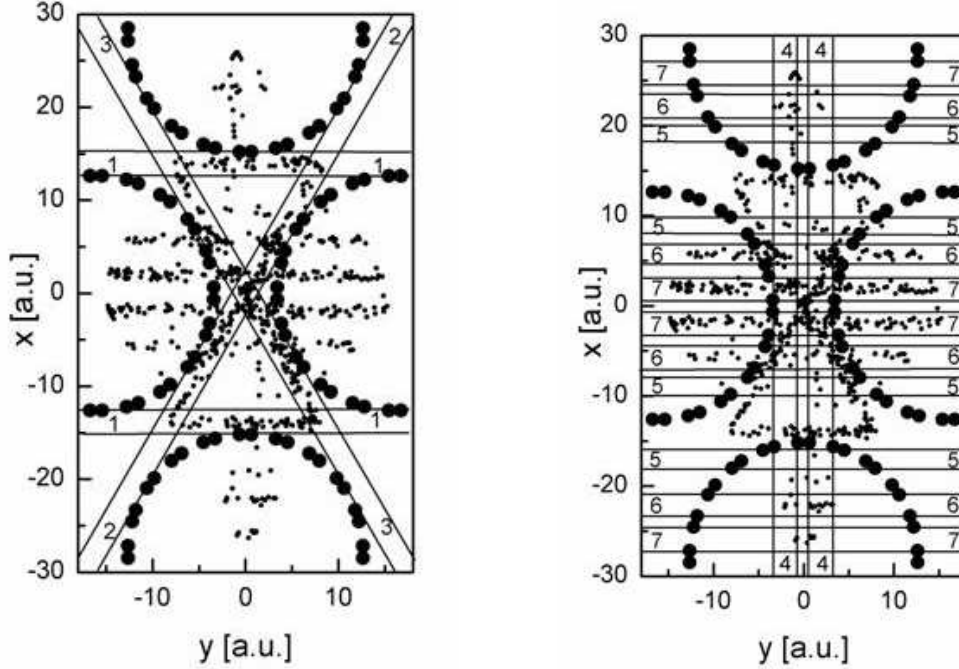


Figure 20: The components of the proton impact parameter vectors, within the primitive cell of the superlattice, that correspond to the arms of the channeling star for the reduced bundle length $\Lambda_2 = 0.65$. (a) The solid lines represent four pairs of planes defined by the atomic strings of the nanotubes, designated by 1, 2 and 3, that enable the planar channeling of the protons through the bundle. (b) The solid lines represent 14 additional pairs of planes defined by the atomic strings of the nanotubes, designated by 4, 5, 6 and 7 that enable the planar channeling of the protons through the bundle.

the (rhombic) primitive cell of the superlattice, that correspond to the arms of the channeling star. They were selected taking that $\Theta \geq 1.0$ mrad. As in the above considered case, the impact parameter vectors are located between seven classes of pairs of parallel lines, representing seven classes of pairs of planes defined by the atomic strings of the nanotubes. There are two equivalent pairs of planes designated by 1, one pair designated by 2 and one pair designated by 3, which are shown in Fig. 22(a), and two equivalent pairs of

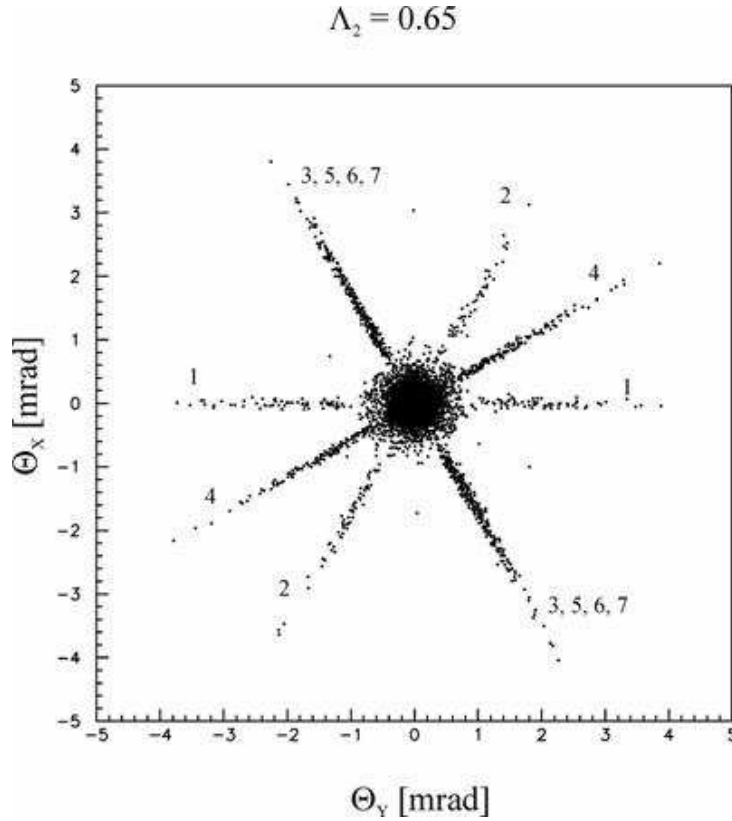


Figure 21: The angular distributions of 1 GeV protons transmitted through the bundle of (10, 10) single-wall carbon nanotubes of the reduced length $\Lambda_2 = 0.65$ when the nanotubes are rotated about their axes by $\pi/60$ counter-clockwise relative to their assumed positions. The proton beam divergence angle is $\Omega_d = 1.884$ mrad.

planes designated by 4, two equivalent pairs designated by 5, two equivalent pairs designated by 6, and two equivalent pairs designated by 7, which are shown in Fig. 22(b). In accordance with this, the arms shown in Fig. 21 are designated by 1, by 2, by 4, and by 3, 5, 6 and 7.

It should be noted that in both of the above considered cases the pairs of planes designated by 1, 2 and 3 do not cross the nanotubes, and that the pairs of planes designated by 4, 5, 6 and 7 cross the nanotubes. Namely, the protons channeled between planes 1, 2 and 3 move only in between the nanotubes while the protons channeled between planes 4, 5, 6 and 7 move

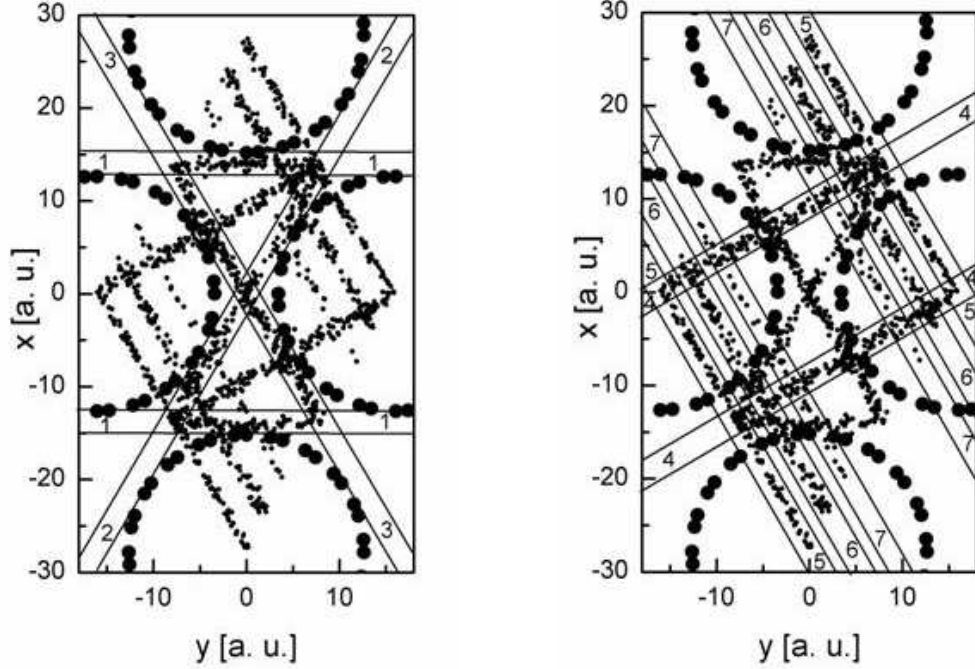


Figure 22: The components of the proton impact parameter vectors, within the primitive cell of the superlattice, that correspond to the arms of the channeling star for the reduced bundle length $\Lambda_2 = 0.65$ when the nanotubes are rotated about their axes by $\pi/60$ counterclockwise relative to their assumed positions. (a) The solid lines represent four pairs of planes defined by the atomic strings of the nanotubes, designated by 1, 2 and 3, that enable the planar channeling of the protons through the bundle. (b) The solid lines represent eight additional pairs of planes defined by the atomic strings of the nanotubes, designated by 4, 5, 6 and 7 that enable the planar channeling of the protons through the bundle.

in between as well as through the nanotubes. Also, it is clear that planar channels 1, 2 and 3 in the former case practically coincide with planar channels 1, 2 and 3 in the latter case. However, planar channels 4, 5, 6 and 7 in the former case considerably differ from the planar channels 4, 5, 6 and 7 in the latter case. This explains the difference between the arrangements of the

arms in these two cases. Thus, one can say that the channeling star effect is sensitive to the mutual orientation of the neighboring nanotubes within a bundle. This means that it is possible to measure the effect and employ the obtained results to determine this orientation.

References

- S. Andersen, K., Fich, O., Nielsen, H., Schitt, H. E., Uggerhøj, E., Vraast Thomsen, C., Charpak, G., Petersen, G., Sauli, F., Ponpon, J. P., Siffert, P., *Nucl. Phys. B*, 1980, *167*, 1
- Appleton, B. R., Erginsoy, S., Gibson, W. M. *Phys. Rev.*, 1967, *161*, 330
- Arista, N. R. *Phys. Rev. A*, 2001, *64* 32901
- Arista, N. R., Fuentes, M. A., *Phys. Rev. B*, 2001, *63* 165401
- Artru, X., Fomin, S. P., Shulga, N. F., Ispirian, K. A., Zhevago, N. K., *Phys. Rep.*, 2005 *412*, 89
- Barrett, J. H. *Phys. Rev. B*, 1971, *3*, 1527
- Barrett, J. H. *Phys. Rev. Lett.*, 1973, *31*, 1542
- Bellucci, S., Biryukov, V. M., Cordelli, A., *Phys. Lett. B*, 2005, *608*, 53
- Berdinsky, A. S., Alegaonkar, P. S., Yoo, J. B., Lee, H. C., Jung, J. S., Han, J. H., Fink, D., Chadderton, L. T. *Nano*, 2008, *2*, 59
- Biryukov, V. M., Bellucci, S., *Phys. Lett. B*, 2002, *542*, 111
- Biryukov, V. M., Chesnokov, YU. A., Guidi, V., Scandale, W., *Nucl. Instrum. Meth B*, 2003, *203*, 236
- Borka, D., Petrović, S., Nešković, N. *J. Electron Spectrosc.*, 2003, *129*, 183
- Borka, D., Petrović, S., Nešković, N., *Mater. Sci. Forum*, 2005, *494*, 89
- Borka, D., Petrović, S., Nešković, N., Mowbray, D. J., Mišković, Z. L. *Phys. Rev. A*, 2006, *73*, 062902
- Borka, D., Petrović, S., Nešković, N., *Phys. Lett. A*, 2006, *354*, 457

- Borka, D., Petrović, S., Nešković, N., Mowbray, D. J., Mišković, Z. L. *Nucl. Instrum. Meth. B*, 2007, *256*, 131
- Borka, D., Mowbray, D. J., Mišković, Z. L., Petrović, S., Nešković, N., *J. Phys.: Condens. Matter*, 2008, *20*, 474212
- Borka, D., Mowbray, D. J., Mišković, Z. L., Petrović, S., Nešković, N., *Phys. Rev. A*, 2008, *77*, 032903
- Borka, D., Petrović, S., Nešković, N., *Techniques: New Materials*, 2008, *17/1*, 9 (in Serbian)
- Borka, D. Mowbray, D.J., Mišković, Z. L., Petrović, S., Nešković, N. *New J. Phys.*, 2010 (accepted)
- Chadderton, L. T. *J. Appl. Crystallogr.*, 1970, *3*, 429
- Chai, G., Heinrich, H., Chow, L., Schenkel, T. *Appl. Phys. Lett.*, 2007, *91*, 103101
- Demkov, Yu. N., Meyer, J. D. *Eur. Phys. J. B*, 2004, *42*, 361
- Saito, R., Dresselhaus G., Dresselhaus, M. S. *Physical Properties of Carbon Nanotubes* (Imperial College Press, London, 2001)
- Doerr, T. P., Yu, Y.-K. *Am. J. Phys.*, 2004, *72* 190
- Doyle, P. A., Turner, P. S. *Acta Crystallogr. A*, 1968 *24*, 390
- Gemmell, D. S. *Rev. Mod. Phys.*, 1974, *46*, 129
- Gevorgian, L. A., Ispirian, K. A., Ispirian, R. K. *Nucl. Instrum. Meth. B*, 1998, *145*, 155
- Greenenko, A. A., Shulga, N. F., *Nucl. Instrum. Meth. B*, 2003, *205*, 767
- Guerret-Piécourt, C., Le Bourar, Y., Loiseau, A., Pascard, H. *Nature*, 1994, *372*, 761
- Hone, J., Batlogg, B., Benes, Z., Johnson, A. T., Fischer, J. E., *Science*, 2000, *289*, 1730
- Iijima, S. *Nature*, 1991, *354*, 56

- Klimov, V. V., Letokhov, V. S. *Phys. Lett. A*, 1996, *222*, 424
- Krasheninnikov, A. V., Nordlund, K., *Phys. Rev. B*, 2005, *71*, 245408
- Krause, H. F., Datz, S., Dittner, P. F., Gomez del Campo, J., Miller, P. D., Moak, C. D., Nešković, N., Pepmiller, P. L. *Phys. Rev. B*, 1986, *33*, 6036
- Krause, H. F., Barrett, J. H., Datz, S., Dittner, P. F., Jones, N. L., Gomez del Campo, J., Vane, C. R., *Phys. Rev. A*, 1994, *49*, 283
- Kwei, C. M., Chen, Y. F., Tung, C. J., Wang, J. P. *Surf. Sci.*, 1993, *293*, 202
- Kwon, Y., Tománek, D. *Phys. Rev. Lett.*, 2000, *84*, 1483
- Lindhard, J., *K. Dan. Vidensk. Selsk., Mat.-Fys. Medd.*, 1965, *34*, No. 14, 1
- Lucas, A. A., Moreau, F., Lambin, Ph. *Rev. Mod. Phys.*, 2002, *74*, 1
- Matyukhin, S. I., Frolenkov, K. Y. *Tech. Phys. Lett.*, 2007, *33*, 58
- Matyukhin, S. I. *Tech. Phys. Lett.*, 2008, *34*, 835
- Miletić, L., Petrović, S., Nešković, N. *Nucl. Instrum. Meth. B*, 1996, *115*, 337
- Miletić, L., Petrović, S., Nešković, N. *Radiat. Eff. Def. Solids*, 1997, *141*, 235
- Mišković, Z. L., *Radiat. Eff. Def. Solids*, 2007, *162*, 185
- Molière, G. *Z. Naturforsch. A*, 1947, *2*, 133
- Moura, C. S., Amaral, L., *J. Phys. Chem. B*, 2005, *109*, 13515
- Moura, C. S., Amaral, L., *Carbon*, 2007, *45*, 1802
- Mowbray, D. J., Mišković, Z. L., Goodman, F. O., Wang, Y.-N. *Phys. Rev. B*, 2004, *70*, 195418
- Mowbray, D. J., Mišković, Z. L., Goodman, F. O., Wang, Y.-N. *Phys. Lett. A*, 2004, *329* 94
- D. J. Mowbray, Z. L. Mišković and F. O. Goodman, *Nucl. Instrum. Meth. Phys. Res. B*, 2007 *256*, 167
- Nešković, N. *Phys. Rev. B*, 1986, *33*, 6030

- Nešković, N., Perović, B. *Phys. Rev. Lett.*, 1987, *59*, 308
- Nešković, N., Kapetanović, G., Petrović, S., Perović, B. *Phys. Lett. A*, 1993, *179*, 343
- Nešković, N., Petrović, S., Živković, L. *Eur. Phys. J. B*, 2000, *18*, 553
- Nešković, N., Petrović, S., Borka, D., Kossionides, S. *Phys. Lett. A*, 2002, *304*, 114
- Nešković, N., Petrović, S. *J. Electron Spectrosc.*, 2003, *129*, 233
- Nešković, N., Petrović, S., Borka, D. *Nucl. Instrum. Meth. B*, 2005, *230*, 106
- Nešković, N., Petrović, S., Borka, D. *Nucl. Instrum. Meth. B*, 2009, *267*, 2616
- Petrović, S., Miletić, L., Nešković, N. *Phys. Rev. B*, 2000, *61*, 184
- Petrović, S., Korica, S., Kokkoris, M., Nešković, N. *Nucl. Instrum. Meth. B*, 2002, *193*, 152
- Petrović, S., Borka, D., Nešković, N. *Nucl. Instrum. Meth. B*, 2005, *234*, 78
- Petrović, S., Nešković, N., Borka, D., *Eur. Phys. J. B*, 2005, *44*, 41
- Petrović, S., Borka, D., Nešković, N., *Eur. Phys. J. B*, 2005, *44*, 41
- Petrović, S., Borka, D., Nešković, N. *Adv. Stud. Theor. Phys.*, 2008, *2*, 415
- Petrović, S., Telečki, I., Borka, D., Nešković, N. *Phys. Lett. A*, 2008, *372*, 6003
- Petrović, S., Borka, D., Telečki, I., Nešković, N. *Nucl. Instrum. Meth. B*, 2009, *267*, 2365
- Press, W. H., Teukolsky, S. A., Vetterling, W. T., Flanery, B. P. *Numerical Recipes in FORTRAN*, University Press: Cambridge, 1993 (p. 547)
- Radović, I., Hadžievski, Lj., Bibić, N., Mišković, Z. L. *Phys. Rev. A*, 2007, *76*, 042901
- Radović, I., Hadžievski, Lj., Mišković, Z. L. *Phys. Rev. B*, 2008, *77*, 075428

- Radović, I., Hadžievski, Lj., Bibić, N., Mišković, Z. L. *Materials Chemistry and Physics*, 2009, *118*, 293
- Robinson, M. T., Oen, O. S. *Phys. Rev.*, 1963, *132*, 2385
- J. Rosner, S., Gibson, W. M., Golovchenko, J. A., Goland, A. N., Wegner, H. E. *Phys. Rev. B*, 1978, *18*, 1066
- Saito, R., Dresselhaus, G., Dresselhaus, M. S. D. *Physical Properties of Carbon Nanotubes*, Imperial College Press: London, 2001
- Swart, J. W., Diniz, J. A., Doi, I., de Moraes, M. A. B. *Nucl. Instrum. Meth. Phys. Res. B*, 2000, *171*, 166
- Thess, A., Lee, R., Nikolaev, P., Dai, H., Petit, P., Robert, J., Xu, C., Lee, Y. H., Kim, S. G., Rinzler, A. G., Colbert, D. T., Scuseria, G., Tománek, D., Fischer, J. E., Smalley, R. E. *Science*, 1996, *273*, 483
- Thom, R. *Structural Stability and Morphogenesis*, Benjamin: Reading, Massachusetts, 1975
- Tsetseris, L., Pantelides, S. T. *Phys. Rev. Lett.*, 2006, *97*, 266805
- Yao, Z., Postma, H. W. Ch., Balents, L., Dekker, C. *Nature*, 1999, *402*, 273
- Zhang, S., Zhao, S., Xia, M., Zhang, E., Xu, T. *Phys. Rev. B*, 2003, *68*, 245419
- Zheng, L.-P., Zhu, Zh.-Y., Li, Y., Zhu, D.-Zh., Xia, H.-H. *J. Phys. Chem. C*, 2008, *112*, 15204
- Zheng, L.-P., Zhu, Zh.-Y., Li, Y., Zhu, D.-Zh., Xia, H.-H. *Nucl. Instrum. Meth. B*, 2008, *266*, 849
- Zhevago, N. K., Glebov, V. I., *Phys. Lett. A*, 1998, *250*, 360
- Zhevago, N. K., Glebov, V. I. *J. Exp. Theor. Phys.*, 2000, *91*, 504
- Zhevago, N. K., Glebov, V. I., *Phys. Lett. A*, 2003, *310*, 301
- Zhu, Zh., Zhu, D., Lu, R., Xu, Zh., Zhang, W., Xia, H., *Proceedings of the International Conference on Charged and Neutral Particles Channeling Phenomena* (Vol. 5974) (SPIE, Bellingham, Washington, 2005), p. 13-1

Živković, L., Petrović, S., Kossionides, S., Nešković, N. *Phys. Lett. A*, 2001, 286, 292